# Characterization of An Exploding Micro-Wire Pulsed Plasma Thruster

Diego Mejia Montano

A thesis
submitted in partial fulfillment of the
requirements for the degree of

Master of Science in Aeronautics & Astronautics

University of Washington

2019

Committee:

Justin M. Little, Chair

Robert Winglee

Program Authorized to Offer Degree:
Aeronautics & Astronautics

University of Washington

## Abstract

Characterization of An Exploding Micro-Wire Pulsed Plasma Thruster

Diego Mejia Montano

Chair of the Supervisory Committee:
Associate Professor Justin M. Little
Aeronautics & Astronautics

Pulsed Plasma Thrusters typically live in the low-range efficiency realm compared to other types of electric propulsion thrusters. In an attempt to explore if any added benefits could be gained from experimenting with a new propellant type, additional physics had to be incorporated into the classical RLC model approach. A study into modeling how a micro-wire propellant would react when subjected to energy deposition via current-driven heating was undertaken. Once a first-order estimate, verified with computational estimates, was obtained then the classical RLC series circuit model could be used to compare and validate the results obtained from experimentation. It was found that while the proposed propellant type is feasible, it produced performance differences that could not be explained solely by the classical model and a more exhaustive investigation into various phenomena will have to be pursued.

# TABLE OF CONTENTS

# LIST OF FIGURES

# LIST OF TABLES

# ACKNOWLEDGMENTS

I would like to personally thank my advisor, Professor Justin Little, for helping carve out a path for me in his newly formed lab group. Similar thanks go out to my lab members – and those outside our small group – for making this process seem much more enjoyable and tenable. All of your assistance was indispensable in helping me put a satisfying conclusion to my graduate education.

# DEDICATION

To my parents and my loved ones.

# Chapter 1

# INTRODUCTION & MOTIVATION

## *1.1 Historical Background*

The feasibility of using a Pulsed Plasma Thruster (PPT) had been experimentally studied since the 1950's by the Soviet Union as an alternative means of propulsion for spacecraft. The first in-flight use of PPTs were the six on board the Soviet Union's Zond 2 Mars surveillance spacecraft launched in 1964. The mission ultimately failed because of lost communications, but the precedent was set and soon the United States also launched their own system in 1968 [1]. The Lincoln laboratory LES-6 satellite successfully operated with the PPT providing station keeping maneuvers during orbital testing. This ignited an interest in the research community attempting to characterize the discharge plasma physics and its salient characteristics. Multiple designs and geometries were also investigated in the hopes of qualifying longer-lasting, more efficient systems.

Since then, PPTs have been researched and developed primarily by universities due to their low costs and complexity when compared to other types of electric propulsion. The main attractive draw of PPTs is their robustness, mechanical simplicity, and their very precise impulse control. These features make it very attractive for use in small payload missions such as a CubeSat launch where occasional and periodic orbital adjustments have to be made.

The drawback to PPTs however is that they are grossly inefficient at converting the given input power into useful directed energy, i.e., thrust to power. At best, PPTs have straddled the 5-10% efficiency range [2].

### *1.2 Progression & Development*

In keeping their relative mechanical complexity to a minimum, most PPTs have not strayed far from the original design. Spring-fed Teflon has been the main stay of choice propellant since it is the only known subliming, ablating, and non-reacting solid that quickly depolymerizes from solid to gas [3]. It is also suitable to exposure in ambient vacuum since it is inert and does not suffer from evaporative losses, thereby not requiring tankage. In relatively recent years however, gaseous and liquid-fed PPTs have been explored where Argon, Xenon, and water have all been studied and comparatively characterized [4]. The drawback is that further engineering consideration for propellant storage and their feed systems have to be taken into account.

In terms of thruster design most, if not all, rely on the two primary electrode configurations: parallel and coaxial gun accelerators. Asymmetric acceleration channels have been built and reportedly improved on the overall efficiency by up to 30-50% [5] when compared to conventional symmetric parallel-plate configurations. Although this is not exclusive to asymmetry as it's been found that even introducing divergence angles to symmetric geometries yields higher thrust to power ratios [6], but eventually suffer from losses if the angle is too aggressive.

The current undertaking as of the time of this thesis is that most of the effort is being spent on trying to find semi-empirical relationships to better describe the discharge process, derive and prove scaling laws, and flight-qualify design improvements for applications in the commercial space sector.

### *1.3 Motivation*

As previously alluded to, PPTs provide very precise orbit and attitude control and this makes them appealing for low-risk scientific or commercial launches. However, while Teflon is easily

ablated it is also a very inconsistent consumer of energy. After vaporization it forms a very complex multi-species plasma containing all sorts of permutations of Carbon and Fluorine atoms and molecules each with varying levels of ionization. This undirected consumption of the given input energy means that there are permanent losses of what could have been useful directed kinetic energy. The process itself is also inconsistent in that the mass slug consumed per shot varies greatly.

So in order to have a more precise consumption of propellant mass per shot a pure elemental substance is preferred. As previously mentioned, gas and liquid-fed PPTs are attractive in that they can be simpler in molecular composition, but make the design more complex. In order to combat this, a compromise between a single species propellant and simplistic engineering is desired. As such, the use of metals delivered in the form of wires was chosen to be the main goal of this study. Metals are attractive in that they are inert, can be exposed to ambient vacuum, and can be precisely fed into a given control volume.

As designated by this thesis, very fine micron-sized diameter wire can be easily purchased and will not require custom ordering or specialized equipment to handle. Likewise the mechanism for feeding it into the ignition zone of the thruster can be handled by a programmed motor to help spool precise lengths.

# Chapter 2

# EXPERIMENTAL SETUP & PROCEDURE

## *2.1 Vacuum Chamber*

The vacuum chamber used in the experiments was a quartz cylinder 2 feet in length with an approximate radius of 5 inches combining to yield a total volume of about 30 liters. It sealed off on both ends via a rubber L-gasket mating with steel plates held together with threaded rods. One of the plates had several ports for interfacing several diagnostics probes and the other plate could mate with the pumping system. The end with the interface to the pumps was connected a turbomolecular pump in series to an oil roughing pump. The end with the connections interface also had a test stand connected to it allowing for experiments to be laid on top of it.

### *2.1.1 Interface Connections*

The plate with the interfaces allowed for passage of custom connections made by passing the required electrical cables through NPT adapters and epoxy sealing the void with Torr Seal. One of these was for the SHV connector cables from the high-voltage power supply to the thruster terminal connections. The power supply was capable of providing up to 5 kV potential. Connected to the power supply leads on the ambient atmosphere side was a Pintech PT-8020 differential high voltage probe. Another one of the adapters was a BNC pass-through for which a Rogowski coil could be connected to. The probe was made from a cut BNC cable with windings around a cable zip-lock tie and then electrically insulated with Kapton tape.

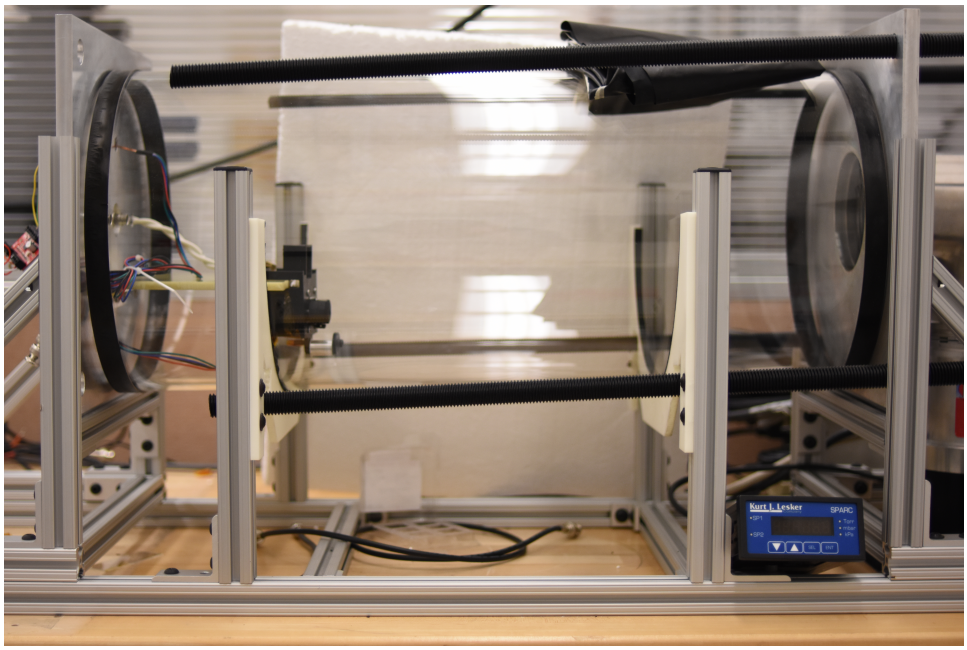


Figure 2.1: Vacuum chamber viewed from the side.

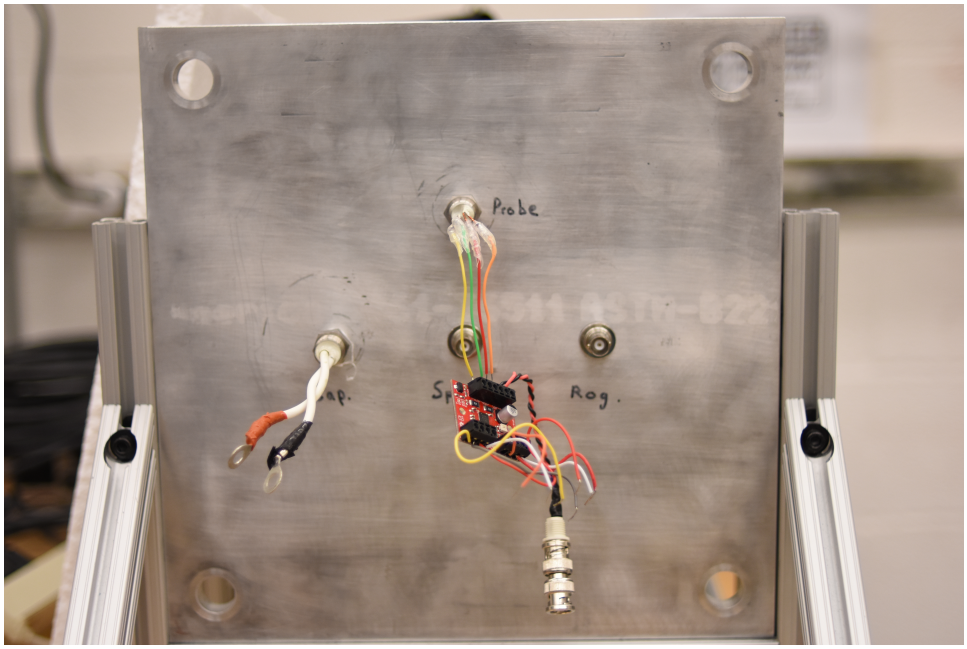


Figure 2.2: Interface plate through which all the main connections were passed.

## *2.2 Diagnostics*

### *2.2.1 Oscilloscope*

The BNC mating to the Rogowski coil as well as the differential high voltage probe were both connected to a 200 MHz Tektonix TDS 2024B series oscilloscope with a 2 GS/s sampling rate. The oscilloscope output data was then collected and stored to a CSV file and transmitted to a computer.

### *2.2.2 High Speed Camera*

A 5 million frames per second, MFPS, high speed Kirana camera was set up and connected to a main control computer. The camera could be varied in its capture rate and could also be triggered to start recording with an input signal. It was set up and connected to provide a side-view of the thruster channel.

## *2.3 Thruster Assembly*

The assembly, Figure 2.3, is composed of a stepper motor, a housing enclosure, and the thruster. The stepper motor is a small NEMA 17 bipolar stepper motor with micro-stepping enabled. It was driven by a Big Easy Driver motor control logic board powered and controlled via an Arduino UNO. The Arduino was programmed to drive the feed rate and direction of the motor as well as send a trigger signal to the Kirana to trigger the recording process.

The housing made for the system was 3D printed to permit the motor and the thruster to both be seated and aligned to each other. At points along the front face of the housing were guiding posts to help the wire follow a set path through the feed system. The housing allowed the motor to be screwed in and secured while permitting the rotating arm to stick out directly below the area the thruster sat in. Concentrically mounted to the rotating motor am was a high-density neoprene rod. Immediately adjacent to that was another neoprene rod which was coupled to the rotation of the other one such that they would both act together

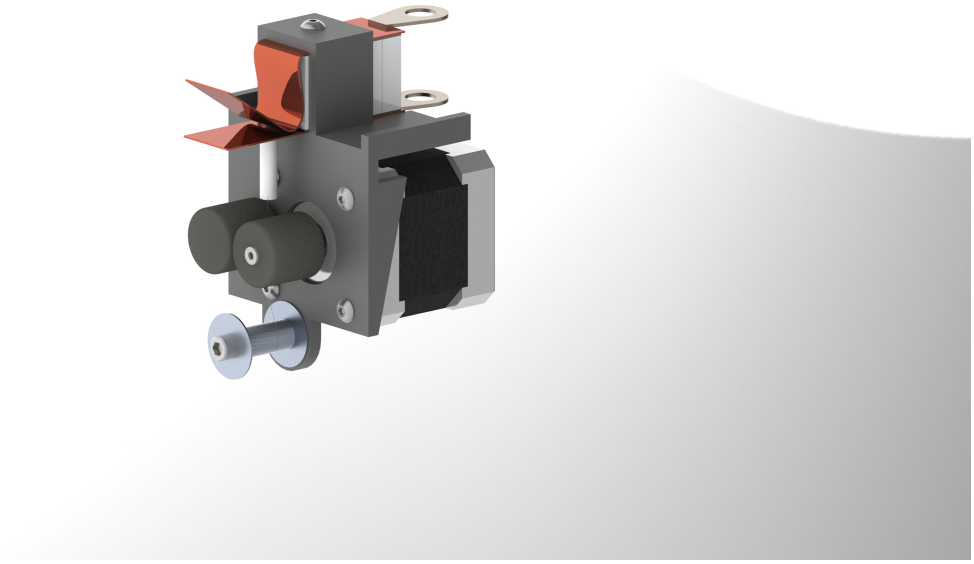

Figure 2.3: Render of the completed thruster assembly.

to pull the wire from the bottom end of the housing. At the bottom of the system was an extension that allowed the wire spool to be sit freely and rotate as the wire was fed by the motor through the guides.

On to the thruster itself, its electrodes are made out of C101 99.99% pure copper that are 0.8128 mm thick. The upper electrode was bent and shaped to permit a Rogowski coil to sit between the capacitor bank as well as to provide a very small inter-electrode spacing where the plasma was created. The lower electrode was not worked aside from having a 1.58 $\pm$ 0.05 mm orifice drilled at the point of smallest inter-electrode spacing. This lowest spacing between the two electrodes was approximately 1.5 $\pm$ 0.05 mm and from this point, the upper plate diverged at an angle of $\sim 22.5°$. The maximum separation was 10 mm. The width of the thruster was the width of the capacitor bank, at about 17.5 $\pm$ 0.1 mm, and the overall

length of the thruster was 65 mm - of which 20.5 $\pm$ 0.1 mm were allotted for the acceleration channel.

Also attached to the bottom electrode was a alumina ceramic guide tube, Figure 2.4, with an inner diameter the same size as the orifice made through the electrode. This was used to help feed the wire and keep it on track should it need to be retracted for any reason. The power stored in the system came from five Novacap Knowles ceramic capacitors, each with 47 nF capacitance, connected in parallel.

### *2.4 Data Reduction Tools*

All the data that was collected, as well as that generated by the models, was processed with Python. Specifically the heavy use of digital signal filters, plotting tools, and numerical calculus packages modules were relied on in this thesis.

### *2.5 Operation Procedure*

The roughing pump would be turned on and the vacuum chamber would evacuate to a pressure of about 300 milliTorr, at which point the turbopump would be turned on and the vacuum chamber would be left for several minutes until its final pressure range of 30-50 $\mu$Torr was achieved. At this stage, the high voltage power supply would be turned on and set it to its operating voltage level to which thruster capacitors would charge almost instantly. The oscillscope was adjusted accordingly and set to trigger upon detection of a falling slope of the voltage signal from the high voltage probe. This was also set for the Rogowski coil channel, but it would instead detect a rising slope. The recording window length of the signals was set to 500 ns. Now, the main control computer would be running the video capturing software as well as as establish a live communications port channel to the Arduino. The camera would then be set to trigger on signal detection and the Arduino channel would receive the feed command. The feed command would then trigger the driver board sending the motor the corresponding amount of steps to rotate and how fast. At this same instance, the Arduino

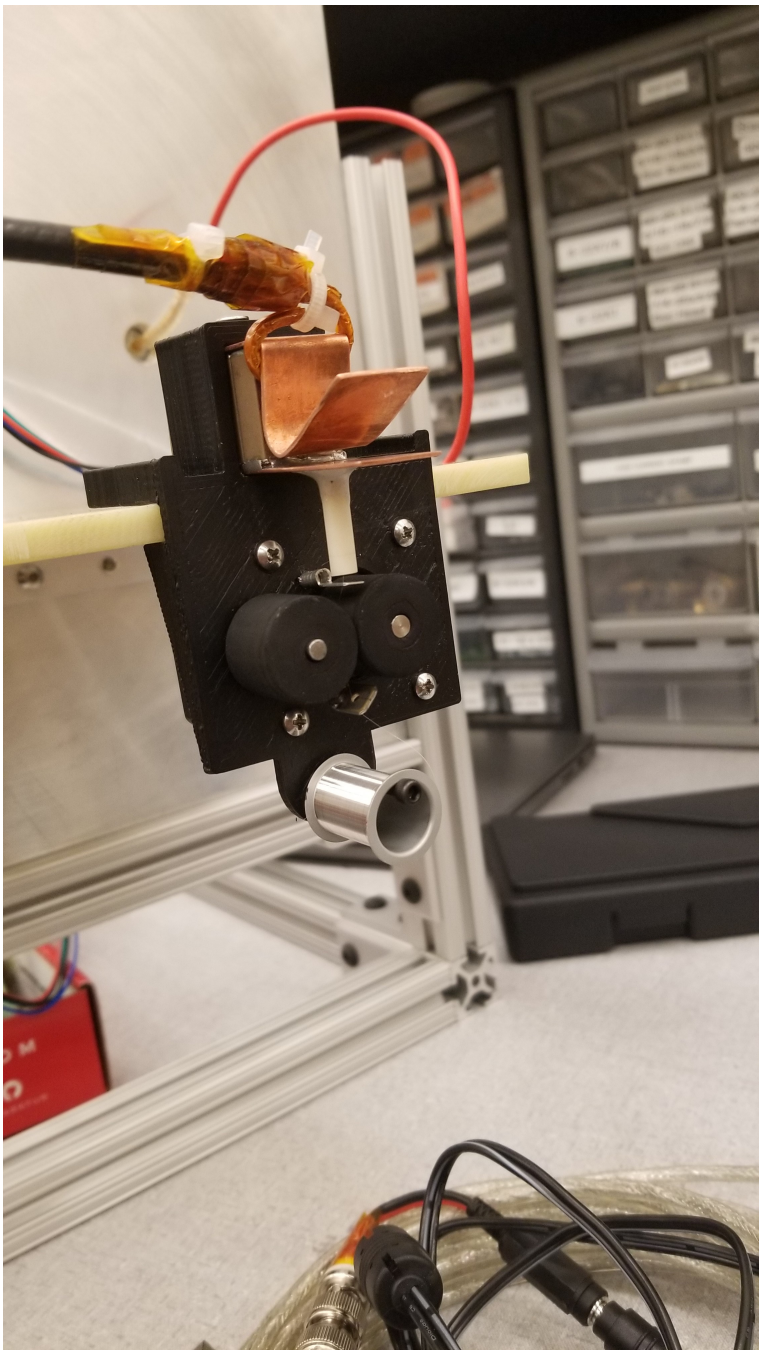

Figure 2.4: A picture of the thruster assembly: housing, thruster, wire, motor, rogowski coil.

also send out a trigger signal to the camera. A time delay between the motor spooling the wire and the camera recording the discharge process had to be manually determined after several test fires. This is because the faster the frame rate was set to, less time was recorded. So a very precise rolling window would be required for faster and faster frame rates. Upon collection of data and successful capture of a single pulse, the process would be repeated until the wire would become stuck.

# Chapter 3

# MODELING AND SCALING OF A WIRE-FED PPT

## *3.1 Multi-Phase Heating Model*

The heating of a wire propellant with constant geometry from solid to plasma is approximated in a three-stage physics process. The solid to gas phase changes are predominantly modeled by the non-constant RLC circuit equation coupled with the respective thermal description of each phase of the propellant. It is in these different regimes that the propellant metal is converting the majority of the available energy deposited by the capacitor bank into thermal energy. With this approach then the primary equations used to describe the physical processes are given by [7][8].

$$L(t)\frac{d^2Q}{dt^2} + \frac{dL}{dt}\frac{dQ}{dt} + R(t)\frac{dQ}{dt} + \frac{Q(t)}{C} = 0 \tag{3.1}$$

$$\rho(T)C_P(T)\frac{\partial T}{\partial t} + \nabla \cdot (\kappa(T)\nabla T) = \dot{q}_V \tag{3.2}$$

Here, the parameters that are dependent on time are $L$ the inductance, $Q$ the charge present in the capacitor bank, $R$ the circuit resistance, and $T$ the temperature of the wire. The parameters that are dependent on temperature are $\rho$ the density, $C_P$ the specific heat capacity, and $\kappa$ the thermal diffusivity. The term $\dot{q}_V$ is the volumetric source heating term driving the temperature change, e.g., Ohmic heating.

In order to simplify the analysis it is noted that equation 3.2 can be reduced from a second order equation to a first order by comparing the magnitude of the spatial derivative with

that of the time derivative, e.g.,

$$\frac{|\nabla \cdot (\kappa(T)\nabla T)|}{|\rho(T)C_P(T)\partial T/\partial t|} \sim \frac{|\kappa\, T/L^2|}{|\rho\, C_P\, T/\tau|} \sim \frac{\alpha\tau}{L^2}$$

The parameter $\alpha$ is the thermal diffusivity, $\tau$ is the characteristic evaporation time scale, and $L$ is the characteristic length of the wire. The characteristic length of the wire is on the order of millimeters, the thermal diffusivity of aluminum found in the literature is on the order of $\mathcal{O}\,(10^{-5})$ [9] [10], and even assuming a very slow ablation time scale on the order of seconds, then

$$\frac{\alpha\tau}{L^2} \sim \frac{10^{-5}\,(1)}{(10^{-3})^2} \sim \mathcal{O}(10^{-1}) \ll 1$$

Meaning that the derivatives for the spatial scales being considered are negligible and thus allowing for the reduction of the heat equation (3.2) to the final form of

$$\rho(T)\, C_P(T)\, \frac{\partial T}{\partial t} = \dot{q}_V \tag{3.3}$$

which reduces the complexity of the computations in the proceeding sections.

### *3.1.1 First Order Ablation Time Estimation*

#### *3.1.1.1 Non-Dimensionalization*

Equations 3.1 and 3.3 are non-dimensionalized in order to try and extract $1^{st}$ order parameters to define scaling laws for a thruster of this kind. Starting with the RLC circuit equation

and assuming constant parameters of inductance and resistance, the parameters $t = t_c t^*$ and $Q(t) = Q_c Q^*(t^*)$ are introduced. Where $t_c$, $Q_c$ are scale factors that allow transformation between the non-dimensional time and charge into their dimensional forms. By looking at one of the initial conditions of equation 3.1, $Q(0) = Q_c Q^*(0) = CV_0$, then the choice of $Q_c = CV_0$ is used such that $Q^*(0) = 1$. Upon their substitution into equation 3.1

$$\frac{d^2Q^*}{dt^{*2}} + \frac{R\,t_c}{L}\frac{dQ^*}{dt^*} + \frac{t_c^2}{LC}\,Q^*(t) = 0$$

It's chosen such that $t_c = \sqrt{LC}$ and the damping ratio per the usual form of $\zeta = (R/2)\sqrt{C/L}$ is followed such that the equation is reduced to the following form with initial conditions

$$\begin{gathered}\frac{d^2Q^*}{dt^{*2}} + 2\zeta\frac{dQ^*}{dt^*} + Q^*(t) = 0 \\ Q^*(0) = 1 \\ \dot{Q}^*(0) = 0\end{gathered}$$

Which upon solving for the non-dimensional charge returns

$$Q^*(t^*) = e^{-\zeta t^*}\left(\cosh\left(t^*\sqrt{\zeta^2-1}\right) + \frac{\sinh\left(t^*\sqrt{\zeta^2-1}\right)}{\sqrt{\zeta^2-1}}\right)$$

and differentiating it such that $J^*(t^*) = -\dot{Q}^*(t^*)$, it is obtained that the dimensionless current is

$$J^*(t^*) = \frac{e^{-\zeta t^*}\,\sinh\left(t^*\sqrt{\zeta^2-1}\right)}{\sqrt{\zeta^2-1}} \tag{3.4}$$

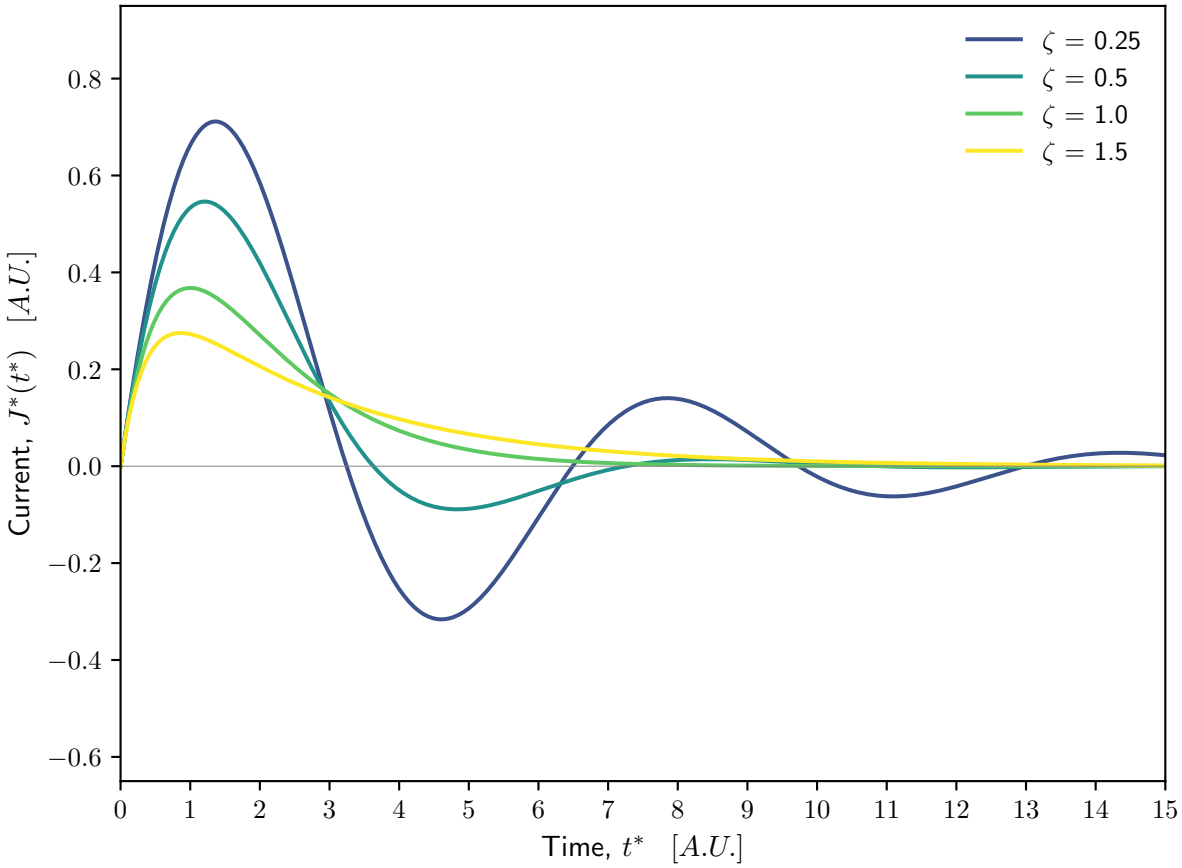


Figure 3.1: Dimensionless current function $J^*(t^*)$ for various damping ratio, $\zeta$, cases.

This current function will model both damped and underdamped responses, but will fail to be analytic for an exact value of $\zeta = 1$, critically damped cases. Numerically entering a value very close to unity, i.e., $\lim \zeta \to 1$, will by-pass this error. The function is plotted for sample cases of damping ratio to demonstrate qualitative behavior in Figure 3.1

Now, turning attention to equation 3.3, we define the volumetric heating term as the internal energy dissipation due to resistance in the wire, namely, $\dot{q}_V = J^2(t)R(t)/V$ where $V$ is the

volume of the material being heated.

By using $J(t) = \dot{Q} = Q_c/tc\,\dot{Q}^*$ we can say that $J(t) = V_0\sqrt{\frac{C}{L}}J^*(t)$ and insert it into the modified heat equation for this problem. As before, we also define a new dimensionless parameter in terms of the temperature, $T = T_c\,T^*(t)$, allowing the heat equation to become

$$\rho(T)\,C_P(T)\,\frac{T_c}{\sqrt{LC}}\frac{\partial T^*}{\partial t^*} = V_0^2\frac{C}{LV}J^*(t)^2\,R(T)$$
$$\frac{\partial T^*}{\partial t^*} = J^*(t)^2\frac{V_0^2\,R\,C^{3/2}}{m_{bit}\,C_P\,L^{1/2}\,T_c}$$

Which makes the choice of the temperature scaling factor

$$T_c = \frac{V_0^2\,R\,C^{3/2}}{m_{bit}\,C_P\,L^{1/2}}$$

Here, $m_{bit}$ is the mass of the material being heated. The resistance and specific heat are functions of temperature but will be assumed to be constants in the section that follows. The non-constant cases will be examined numerically in the proceeding sections. After doing so, this ultimately leaves the non-dimensional form of the heat equation with the following initial condition

$$\frac{\partial T^*}{\partial t^*} = J^*(t^*)^2 \quad \text{with} \quad T^*(0) = \frac{T_0}{T_c}$$

Where the initial temperature is taken to be room temperature for this experiment, i.e., $T_0 = 293$ K.

*3.1.1.2 Heating parameter*

In the initial process of heating the solid wire and phase-changing the propellant into its liquid phase and subsequently gaseous phase, it's noted that the current is the driver of the whole process and by Taylor expanding the function (3.4) about the $t^* = 0$ point

$$J^*(t^*) = t^* - \zeta t^{*2} + \left(\frac{2\zeta^2}{3} - \frac{1}{6}\right) t^{*3} + ...$$

Now, since this power series is dependent on successive powers of time, we assume that the time necessary to ablate a thin wire will be very fast, i.e., $\mathcal{O}(t) \ll 1$ s. With this in hand, any higher order approximations will only marginally change the error of the first order approximation. This then allows the integration of the non-dimensional heat equation

$$\begin{aligned} \int_{T_0^*}^{T_f^*} dT^* &\approx \int_0^{t_f^*} t^{*2} dt^* \\ \Delta T^* &= \frac{1}{3} t_f^{*3} \\ t_f^* &= (3\Delta T^*)^{1/3} \end{aligned}$$

whereby now the nondimensional parameters can be converted back to dimensionalized ones. At this step. the substitution of $R = \xi\,\ell/A$ and $m_{bit} = \rho\pi r^2 \ell$ is made. Where $\xi$ is the material resistivity, $\ell$ is the length of the wire, $A$ is its cross-sectional area, and $r$ is its radius. These substitutions then lend themselves to obtain the following parameter

$$t_f = \left[\alpha \left(\frac{L^2 r^4}{V_0^2}\right)\right]^{1/3}$$

$$\alpha = \frac{3\pi^2 \Delta T\, \rho\, C_P}{\xi}$$

The parameter $\alpha$ is purely a property of the material in use and has units of J $\Omega^{-1}$ $m^{-4}$. In this case it is beneficial to minimize $\alpha$ in design practices such the evaporation of the material is achieved faster. As mentioned prior however, the values of density, specific heat, and resistivity will all change with temperature. So in order to get an upper bound on vaporization times, it is chosen that using the maximum values of density and specific heat, and the lowest possible resistivity, will yield the highest possible value of $\alpha$ that can occur over the heating process. Thus it would provide a better estimate for the slowest possible vaporization time of any given material.

In the literature, it is found that the specific heat of aluminum during its solid and liquid phases will reach a maximum value of $C_P = 1180$ J $kg^{-1}$ $K^{-1}$. For its density, room temperature density is the maximum value it will obtain, $\rho = 2700$ kg $m^{-3}$, during the set of experiments. Similarly, a room temperature resistivity means a minimum value of $\xi = 26.5$ n$\Omega$·m is used. Now, taking the boiling point of Aluminum at standard temperature and pressure, STP, so $\Delta T = (2743 - 293)$ K, then it can be calculated that $\alpha = 8.72 \cdot 10^{18}$ J $\Omega^{-1}$ $m^{-4}$. Using the above calculated numbers, a plot of estimated ablation times for aluminum can be determined as a function of input voltages. Assuming a stray inductance of $L = 10$ nH, the expected value of the completed thruster, and the wire radius of $r = 12.7\,\mu$m, it is seen in Figure 3.2 that ablation times occur on a scale comparable to tens of nanoseconds.

### *3.1.2 Numerically Estimating Ablation Times*

In order to gauge the effectiveness of the first order approximation, a study of the thermodynamic properties of Aluminum is performed. Finding information pertaining to the resistivity [11][12] and specific heat capacity [13] of the metal is readily found in the literature. This data is then collected and curve-fitted using interpolated cubic splines. They are then plotted with respect to a wide range of temperatures in Figures 3.3 and 3.4. These fits can then be

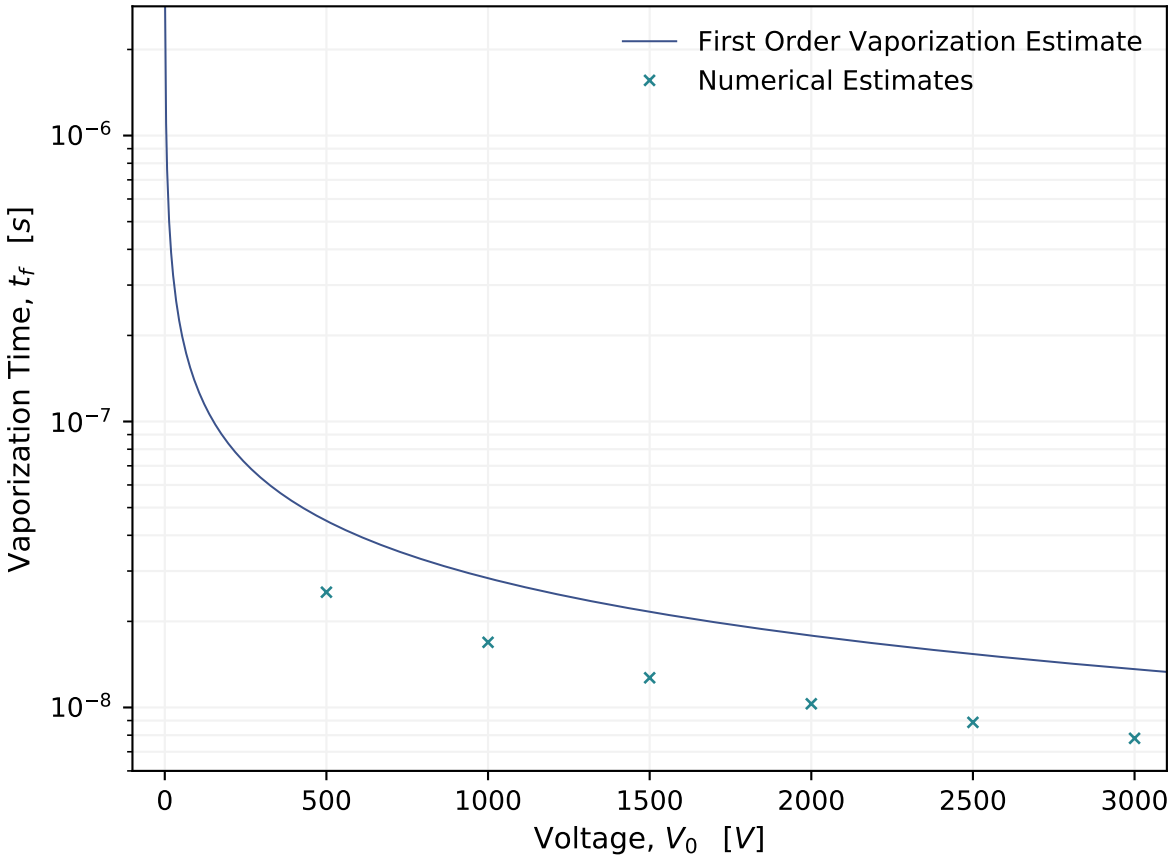


Figure 3.2: Estimated ablation times for an aluminum wire with radius of 12.7 $\mu$m.

used to obtain the values at a given temperature and phase of the metal.

Having these fits to the data, attention is once again returned to equations (3.1) and (3.3) where numerical integration is performed to obtain the temperature profile as a function of time. Looking at Figure 3.5, it is shown that with the inclusion of temperature dependence on the resistivity and specific heat, the vaporization time decreases with increases in voltages.

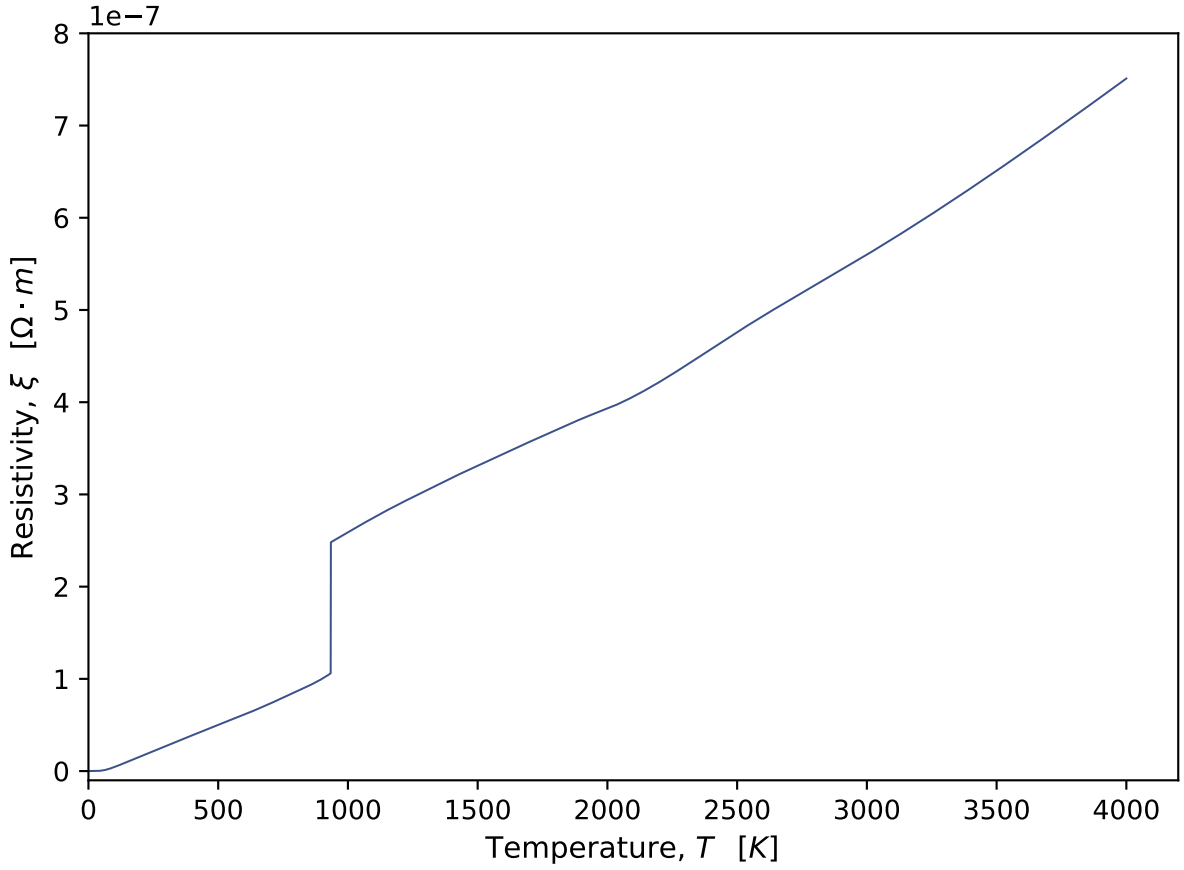


Figure 3.3: Curve fitted data of resistivity of Aluminum for a broad range of temperatures.

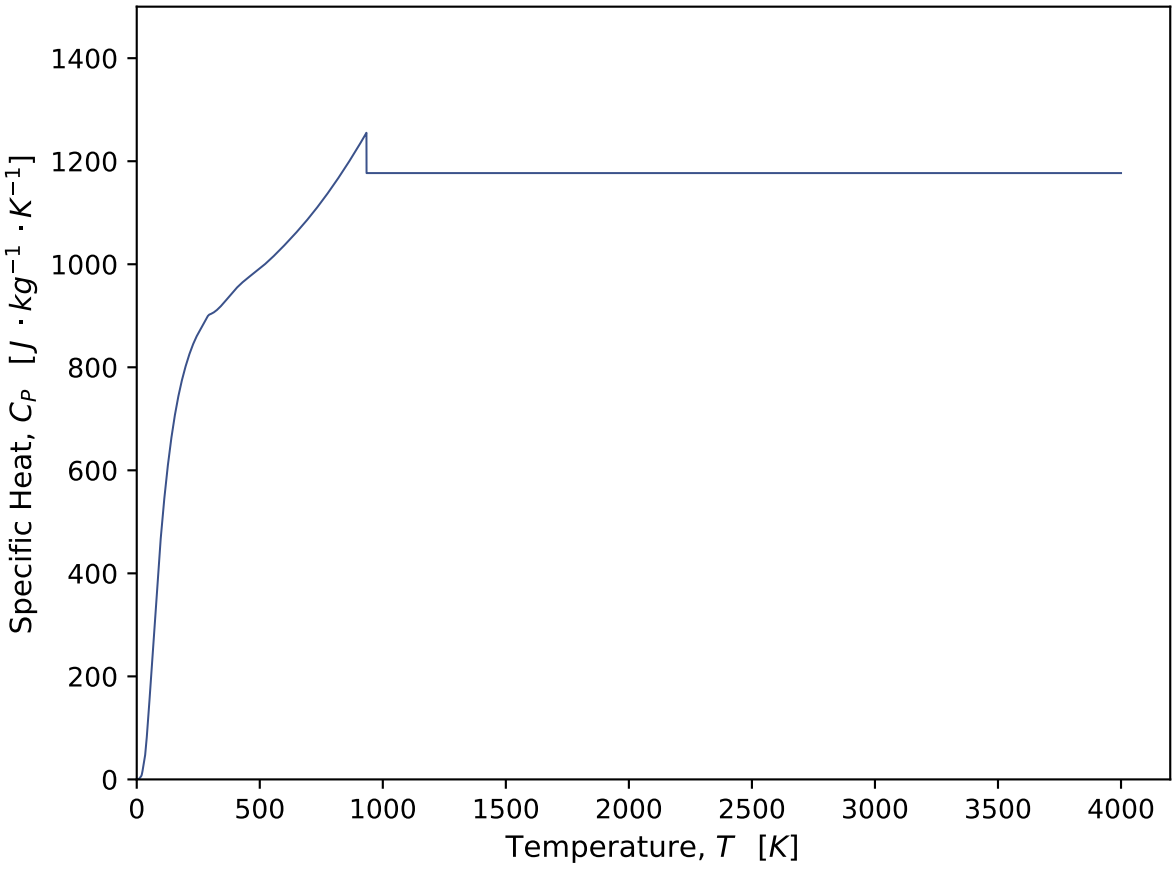


Figure 3.4: Curve fitted data of specific heat capacity of Aluminum for a broad range of temperatures.

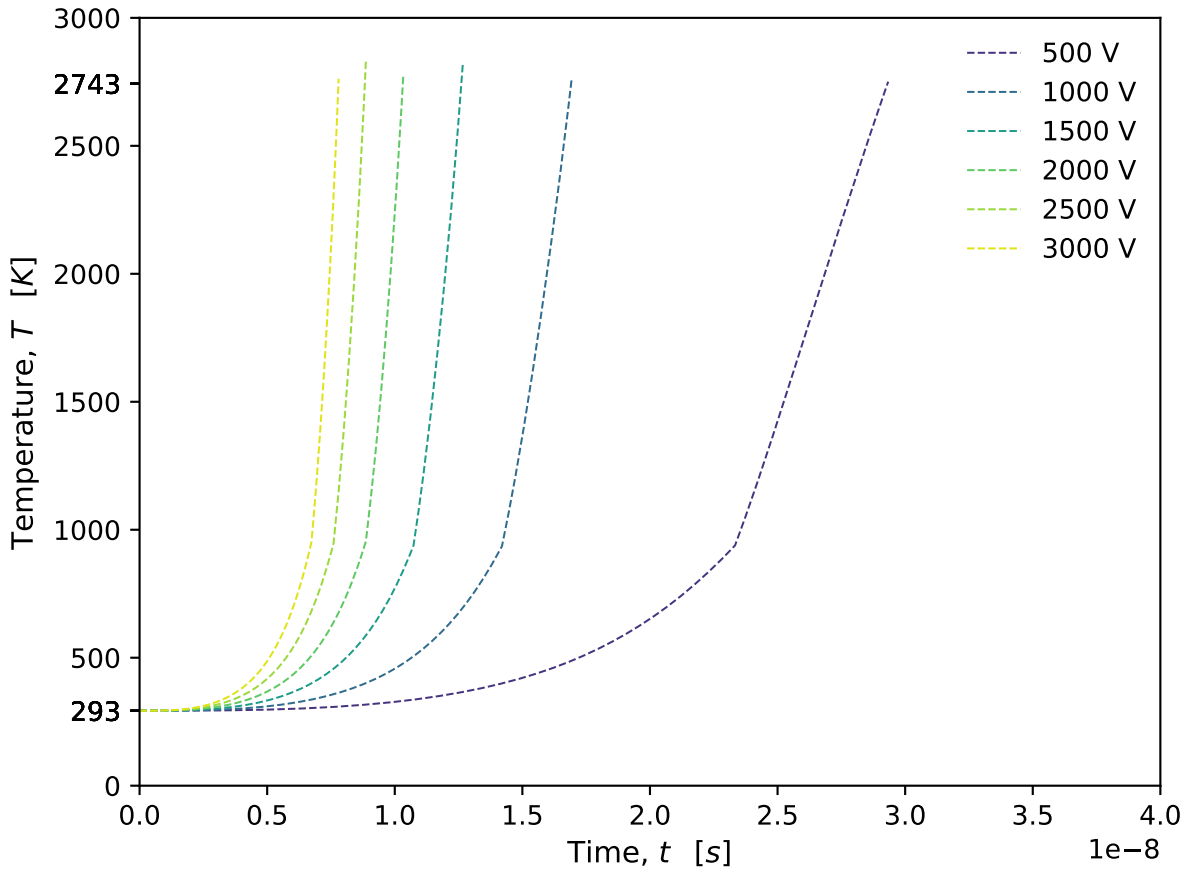


Figure 3.5: Numerically integrated curve estimating temperature rise of Aluminum until its boiling point.

One feature that is apparent from the integrated data curve is the sharp kink where the temperature has a drastic increase over a span of time much shorter than the initial ramp-up period. This is due to the transition at which solid Aluminum turns into its liquid phase as the resistivity more than doubles, Figure 3.3, and the specific heat stays constant, Figure 3.4.

Looking at Figure 3.5, for an initial potential of 1 kV it takes about 15 ns for vaporization. For 2 kV approximately 7.5 ns. And for 3 kV, approximately 6 ns. These numerically obtained numbers are even smaller than those predicted by the first order approximation show in Figure 3.2, by a factor of about one half. But, they are still on the same order of magnitude which lends to provide the first order approximation as a tool for getting a rough, order estimate on wire vaporization times. These values are also shown as data points in Figure 3.2 to demonstrate how they compare to the first order approximation time. This also helps verify that the first order time is purposely meant to over-predict the vaporization times of the wire.

### *3.2 Coupled Description of Plasma Sheet Kinematics*

Once the wire is has expended enough thermal energy from the electrical pulse due to Ohmic heating, it can begin accelerating due to the Lorentz force created by the self-induced magnetic field. Following in the same vein of circuit analyses of pulsed plasma accelerators as referenced in Jahn [7], it is assumed that the plasma is decidedly created as soon as the wire vaporizes and it is immediately entrained in a sheet that traverses the channel until ejected. Thus, the plasma is acting as a switch for the circuit characterized by equation (3.1). This model is effective at predicting the discharge process of the circuit as well as lend some estimates on velocity of the sheet.

In Figure 3.6, $B$ is the magnetic field, $h, d$ are the channel height and width, respectively, $j$ is the current density through the sheet, $\dot{x}$ is the velocity of the sheet, and $\delta$ is the discrete

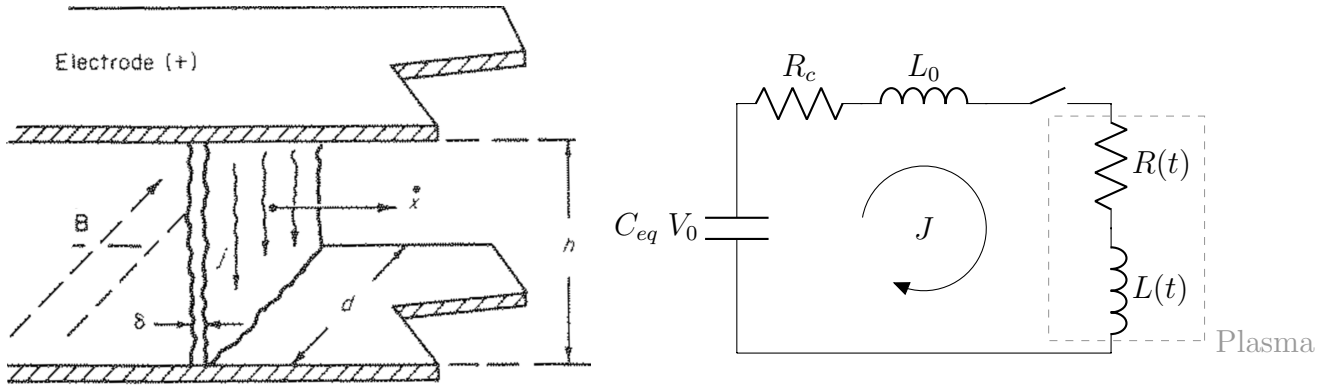


Figure 3.6: Schematic of the plasma-completed circuit [7] and its representative circuit diagram.

sheet's thickness. This first assumption, a discrete and sheet-defined plasma, allows us to effectively ignore any snowplowing effects, i.e., any slow accumulation of entrained particles as the sheet propagates down the channel. The second assumption is that as the plasma is created and is, as a whole, already singly ionized. This specifies that the plasma can then be modeled as a fluid with resistivity estimated by the Spitzer formula [14] after taking into account the over-estimation factor of 2

$$\eta = \frac{m_e^{1/2}\, Z\, e^2\, \ln\Lambda}{2^{1/2}\, 12\, \pi^{3/2}\, \epsilon_0^2\, T_e^{3/2}} \tag{3.5}$$

Where $m_e$ is the electron mass, $Z$ is the effective ionization level, $e$ is the fundamental charge, $\ln\Lambda$ is the Coulomb logarithm, $\epsilon_0$ is the vacuum permittivity, and $T_e$ is the plasma temperature in Joules. This resisivity demonstrates that the plasma temperature is wholly dependent on its temperature. If $Z = 1$ is taken, singly ionized, then the expression can then be cast as function of temperature in units of eV, i.e., $\eta = 5 \cdot 10^{-5}\, \ln\Lambda\, T_e[\text{eV}]^{-3/2}$ where it is evident that as the plasma temperature increases, its resistivity tends to zero.

Assuming that on average a plasma temperature of $T_e = \mathcal{O}(1)$ eV will be observed during the

set of experiments, e.g. a cold plasma as typically produced by PPTs, then the resistivity is approximately $\eta = 7.5 \cdot 10^{-4}\,\Omega\,\mathrm{m}$ which is demonstrably higher than most pure metals. But, taking this and running with the initial assumption of a discrete plasma sheet and generously assuming an aspect ratio $\ell/A \approx 44$, i.e., a 2 mm thick $\times$ 17 mm wide area spanning the throat with a height of 1.5 mm, the resistance contribution of the plasma is $R_p \approx 30\,\mathrm{m}\Omega$ at max. Compared to the overall equivalent resistance of the circuit $R_c \approx 20\,\mathrm{m}\Omega$, this allows then to treat the resistance as constant and defined by the sum of these resistive elements. Knowing this then it is anticipated that the RLC model will produce comparable results with this as an input condition.

By similar argument, one can assert that the changing inductance of the circuit, $L(t)$, can be taken as the initial total inductance when shorted by the propellant plus the effects of the accelerating plasma sheet down the electrodes - in essence, increasing the inductance for every unit length of distance traveled by the sheet. Mathematically speaking,

$$L(t) = L_0 + L_1\,x(t), \qquad L_1 = \mu_0\,\frac{h}{d}$$

Where $L_0$ is the initial total inductance of the circuit, $L_1$ is the inductance per unit length, $x(t)$ is the position of the sheet at some point in time, and $\mu_0$ is the vacuum permeability. Having this relationship and knowing $J(t) = -\dot{Q}$, equation (3.1) is expanded to obtain

$$[L_0 + L_1\,x(t)]\,\ddot{Q}(t) + (L_1\dot{x})\,\dot{Q} + R_c\,\dot{Q} + \frac{Q(t)}{C} = 0$$

Now, Newton's Law of motion is introduced and assuming that the principal acceleration mechanism is provided by the Lorentz force over the discrete plasma sheet volume [7]

$$m_{bit}\,\frac{d\dot{\mathbf{x}}}{d\,t} = \int_V (\vec{j}\times\vec{B})\,dV$$

Where $m_{bit}$ is the accelerated mass bit of the thruster. Referencing Figure 3.6, it is apparent that the product of the curl is aligned with $\dot{\mathbf{x}}$, hence the vector notation will be dropped. Now using Ampere's Circuital Law

$$\oint_\ell \vec{B}\cdot d\vec{\ell} = \mu_0 \int_A \vec{j}\cdot d\vec{A}$$
$$2B_z d = \mu_0\, d \int_0^\delta j_y\, dx$$

and the relationship between total current and current density,

$$J = \int_A \vec{j}\cdot d\vec{A}$$
$$J = d\int_0^\delta j_y\, dx$$

Which can both now be substituted back into Newton's law to yield

$$m_{bit}\,\ddot{x} = \iiint_V (j_y B_z)\,dxdydz$$
$$\ddot{x} = \frac{1}{m_{bit}} hd \int_0^\delta j_y \left[\frac{\mu_0}{2}\int_0^\delta j_y\,dx\right]\,dx$$
$$\ddot{x} = \frac{1}{2m_{bit}}\mu_0\, hd\,\left[\int_0^\delta j_y\,dx\right]^2$$
$$\ddot{x} = \frac{1}{2m_{bit}}\frac{\mu_0\, h}{d}\,J^2$$
$$\ddot{x} = \frac{1}{2m_{bit}} L_1\,J^2$$

This set can now be reduced and set up as a system of ordinary differential equations by combining it with equation (3.1) and introducing the following substitution variables

$$\begin{bmatrix} Q \\ \dot{Q} \\ V \\ x \\ \dot{x} \end{bmatrix} = \begin{bmatrix} P \\ P_0 \\ P_1 \\ P_2 \\ P_3 \end{bmatrix} \quad \Longrightarrow \quad \begin{bmatrix} \dot{Q} \\ \ddot{Q} \\ \dot{V} \\ \dot{x} \\ \ddot{x} \end{bmatrix} = \begin{bmatrix} \dot{P} \\ \dot{P}_0 \\ \dot{P}_1 \\ \dot{P}_2 \\ \dot{P}_3 \end{bmatrix}$$

Where the voltage across the rails is described by the relationship $V(t) = Q(t)/C$ and $\ddot{x}(t) = \dot{v}(t)$ such that

$$\begin{bmatrix} \dot{Q} \\ \dot{J} \\ \dot{V} \\ \dot{x} \\ \dot{v} \end{bmatrix} = \begin{bmatrix} \dot{P} \\ \dot{P}_0 \\ \dot{P}_1 \\ \dot{P}_2 \\ \dot{P}_3 \end{bmatrix} = \begin{bmatrix} P_0 \\ \frac{-1}{L_0 + L_1 P_2}\left(P_1 + P_0 R_c + L_1 P_0 P_3\right) \\ P_0/C \\ P_3 \\ \frac{1}{2m_{bit}} L_1 \, P_0^2 \end{bmatrix} \qquad \begin{bmatrix} Q_0 \\ J_0 \\ V_0 \\ x_0 \\ v_0 \end{bmatrix} = \begin{bmatrix} Q \\ 0 \\ Q/C \\ 0 \\ 0 \end{bmatrix} \tag{3.6}$$

Which yields a system of ODEs that can be numerically solved with an explicit forward-time scheme. For the purpose of this thesis, the adaptive Runge-Kutta 5(4) method was employed.

### *3.3 Design and Scaling Laws*

In order to predict how the thruster would perform as parameters were varied, several aspects of the circuit, materials, and dimensions had to be iterated over several times to reach a general understanding of how each parameter influenced the other.

### *3.3.1 Thruster Dimensional Constraints*

To begin with, this thesis was birthed in the hopes of outlining the usefulness of alternative solid propellants for use in CubeSAT missions. Its purpose was to determine whether said novel propellants could provide efficiencies on par, or greater than, other flight-proven PPTs. As such, the design required something very compact. Since CubeSATs are at their smallest 1U (100 mm $\times$ 100 mm $\times$ 100 mm) the thruster would have to be smaller than these length scales. It would also need to be modular enough that it didn't have to rely on external passive electrical components.

### *3.3.2 Wire Material Considerations*

As reviewed in subsection 3.1.1.2, the main factors in predicting wire vaporization time were the voltage levels, total inductance of the circuit, its radius, and some thermodynamic properties of the materials. The first design criteria was for developing an upper bound on material vaporization times to create a plasma. To complement this requirement, it was also sought to minimize the mass of the vaporized wire, thus maximizing $\dot{v}$, in equation 3.6. Referring to Table 3.1, it can be seen that although Aluminum was among the slowest to vaporize, it is the least dense of all the materials. Having chosen this, the next step was finding the smallest possible radius of wire that could be purchased off-the-shelf. Wire manufacturer Bonding Source had in-stock availability of a 25.4 $\mu$m diameter wire, the smallest available wire that could be found.

### *3.3.3 Passive Components and Energy Requirements*

Next up is the selection of capacitors. This task is one of the most defining criteria for a thruster of this kind since the capacitor bank had to be able to hold enough energy, fit the dimensional constraints, and withstand the high currents and voltages seen during PPT operation. This process should try to optimize the total energy storage while minimizing capacitor dimensions. This project used a total of 5 Novacap, $C = 47$ nF, with a maximum

Table 3.1: Estimated vaporization times and thermodynamic properties at STP for various metals using an initial voltage of 1000 V and inductance of 10 nH.

| | $\rho$ | $\xi$ | $C_P$ | $\alpha$ | $t_v$ |
|---|---|---|---|---|---|
| | kg m$^{-3}$ | n$\Omega$·m | J kg$^{-1}$ K$^{-1}$ | J $\Omega^{-1}$ m$^{-4}$ | ns |
| Aluminum | 2700 | 26.5 | 1180 | $8.72{\cdot}10^{18}$ | 28.3 |
| Copper | 8960 | 15.4 | 385 | $16.8{\cdot}10^{18}$ | 35.2 |
| Iron | 7874 | 96.1 | 449 | $3.10{\cdot}10^{18}$ | 20.0 |
| Nickel | 8908 | 69.3 | 444 | $4.58{\cdot}10^{18}$ | 22.8 |
| Zinc | 7140 | 59.0 | 390 | $1.23{\cdot}10^{18}$ | 14.8 |

breakdown voltage of 3 kV and maximum 3 kA current capability per capacitor. This allowed for energies between $\mathcal{O}(10^{-1})$ J and $\mathcal{O}(1)$ J delivered per pulse, ensuring that there be enough useful energy for in-space propulsion.

### *3.3.4 Thruster Performance Scaling*

In consideration of all the above and having selected first the capacitors which dictated the maximum height and width of the thruster, the next step was figuring out the material to build the electrodes with. Since copper has the lowest resistivity of common metals and is low-cost on top of being easy to form and shape, it was selected as the electrode material. Now, since the initial inductance contributes to a longer LC time, i.e., peak current occurs over this period, then a higher initial inductance seems desirable. But not so much that it overshadows the effects of increasing inductance as the sheet traverses the channel, [7], because the increasing induction contributes to efficiencies in accelerating the plasma sheet. It is apparent then that these two need meticulously controlled in the design of the circuit. But, another important yet conflicting factor is that the smaller the plate separation, the

less mass introduced into the channel. To reconcile these two pieces of information, the thruster was designed such that there would be a throat with minimum possible height to allow for observation and troubleshooting and an exaggerated diverging channel to increase the inductance. Unintendedly, this also probably contributes to efficiencies not related to plasma dynamics, but established gas-dynamic expansion properties.

With this it was decided that a miniminum throat height of 1.5 mm would allow for visibility of the wire and also allow small tools to perform cleaning should any materials be stuck or welded near the throat. This in turn sets the mass of the wire to enter the channel and allows calculations of all the following propellant properties

Table 3.2: Mass bit calculations of an Aluminum wire.

| Aluminum Wire Properties | | |
|---|---|---|
| $r$ | 12.7 | $\mu$m |
| $\ell$ | 1.5 | mm |
| $V_{wire}$ | $7.6{\cdot}10^{-13}$ | $m^3$ |
| $m_{bit}$ | $2.05{\cdot}10^{-9}$ | kg |
| $\alpha$ | $8.72{\cdot}10^{18}$ | J $\Omega^{-1}$ $m^{-4}$ |

Table 3.3: Circuit parameters of the PPT system.

| Power Supply and Circuit | |
|---|---|
| $C$ | 235 nF |
| $L_0$ | 10 nH |
| $R_c$ | 10 mΩ |
| $R_{wire}$ | 78 mΩ |
| $I_{max}$/Cap | 3 kA |
| $V_{max}$/Cap | 3 kV |
| LC time | 373 ns |
| L/R time | 191 ns |
| $\zeta$ | 0.2 |

Since the vaporization time has been characterized with a scaling law presented in equation (3.2), other scaling relationships are examined. First, recalling that since it was earlier found that $J(t) = V_0\sqrt{\frac{C}{L}}J^*(t)$, then the maximum possible current could be when $J^*(t) = 1$, therefore

$$J_{max} = V_0\sqrt{\frac{C}{L}}$$

To estimate the remaining voltage at the time of wire vaporization, the non-dimensional charge equation is multiplied by its scale factors, $Q_c = CV_0$ and $t_c = \sqrt{LC}$ and then approximated via a Taylor expansion as

$$Q(t) = (CV_0)\, e^{-\zeta t/\sqrt{LC}} \left( \cosh\left( \frac{t}{\sqrt{LC}} \sqrt{\zeta^2 - 1} \right) + \frac{\sinh\left( \frac{t}{\sqrt{LC}} \sqrt{\zeta^2 - 1} \right)}{\sqrt{\zeta^2 - 1}} \right)$$

$$Q(t) = CV_0 \left( 1 + \frac{1}{2LC} t^2 + \dots \right)$$

Such that we can approximate the voltage as

$$V(t) \approx V_0 \left( 1 + \frac{1}{2\,LC} t^2 \right)$$

Now a characteristic velocity is defined as the exhaust velocity achieved if the thruster is completely efficient in converting the remaining post-vaporization voltage, $V_v$, into acceleration of the plasma sheet. This is defined as

$$\frac{1}{2} C V_v^2 = \frac{1}{2} m_{bit}\, v_{char}^2$$

$$v_{char} = V_v \sqrt{\frac{C}{m_{bit}}}$$

And lastly, to complete the design of the thruster channel length we assume a characteristic length, $l_{char} = v_{char}\, \tau$, where $\tau$ is the approximate span of time it takes for the energy to be dissipated in the circuit. For this purpose, the L/R time constant is assumed since it naturally captures the dissipative properties of an RL circuit and help to provide a rough estimate on how long it takes for the circuit to ring out. With a factor of $5\tau$ it is obtained that

$$l_{char} = 5\, v_{char} \frac{L}{R}$$

With all this information in tow, a table showing how the thruster is expected to perform according to the scaling laws is generated and presented in Table 3.4. It takes given input voltages and calculates the expected wire vaporization times, maximum achieved current, remaining post-vaporization voltage $V_v$, expected characteristic velocity, and lastly, the necessary characteristic length of the acceleration channel required to completely expend all the energy in a pulse firing. This analysis now fully describes a wire-fed pulsed plasma thruster. These parameters could easily be swapped out for properties of other materials, different thruster geometries, and other circuit component values to help yield estimations on thrusters that consume metallic wire propellants.

Referring to Table 3.4, the cells which are shaded in represent values of the respective parameter which fail to meet a certain design criteria. Specifically, ablation times that are not 5 times faster than the minimum of either the LC time or the L/R time. This is because those ablation times are considered way too slow to leave enough energy in the circuit to function as an effective thruster. Effective voltages less than 1 kV were also discarded. Lastly, any exhaust velocity that was less than 20 km per second was also considered ineffective for in-space use.

Table 3.4: Table of scaling laws demonstrating salient thruster performance characteristics.

| $V_0$ | $E_0$ | $t_v$ | $I_{max}$ | $V_v$ | $v_{char}$ | $\ell_{char}$ |
|---|---|---|---|---|---|---|
| V | J | ns | kA | V | km s$^{-1}$ | mm |
| 1000 | 0.12 | 28.3 | 4.85 | 996 | 10.7 | 6.79 |
| 1100 | 0.14 | 26.6 | 5.33 | 1096 | 11.7 | 7.47 |
| 1200 | 0.17 | 25.1 | 5.82 | 1196 | 12.8 | 8.16 |
| 1300 | 0.20 | 23.8 | 6.30 | 1296 | 13.9 | 8.84 |
| 1400 | 0.230 | 22.6 | 6.79 | 1396 | 14.9 | 9.52 |
| 1500 | 0.26 | 21.6 | 7.27 | 1496 | 16.0 | 10.21 |
| 1600 | 0.30 | 20.7 | 7.76 | 1596 | 17.1 | 10.89 |
| 1700 | 0.34 | 19.9 | 8.24 | 1696. | 18.2 | 11.57 |
| 1800 | 0.38 | 19.1 | 8.73 | 1796 | 19.2 | 12.25 |
| 1900 | 0.42 | 18.5 | 9.21 | 1897 | 20.3 | 12.94 |
| 2000 | 0.47 | 17.8 | 9.70 | 1997 | 21.4 | 13.62 |
| 2100 | 0.52 | 17.3 | 10.2 | 2097 | 22.4 | 14.30 |
| 2200 | 0.57 | 16.7 | 10.7 | 2197 | 23.5 | 14.98 |
| 2300 | 0.625 | 16.2 | 11.1 | 2297 | 24.6 | 15.66 |
| 2400 | 0.68 | 15.8 | 11.6 | 2397 | 25.6 | 16.35 |
| 2500 | 0.73 | 15.4 | 12.1 | 2497 | 26.7 | 17.03 |
| 2600 | 0.79 | 15.0 | 12.6 | 2597 | 27.8 | 17.71 |
| 2700 | 0.86 | 14.6 | 13.1 | 2697 | 28.9 | 18.39 |
| 2800 | 0.92 | 14.3 | 13.6 | 27967 | 29.9 | 19.08 |
| 2900 | 0.99 | 13.9 | 14.1 | 2897 | 31.0 | 19.76 |
| 3000 | 1.06 | 13.6 | 14.5 | 2997 | 32.1 | 20.44 |

# Chapter 4

# DATA ANALYSIS & DISCUSSION

## *4.1 Data Conditioning*

The large sets of data collected for each incremented voltage level needed to be processed/smoothed such that the fits retained the corresponding salient characteristics of the original data. One major variability of this thruster and of PPTs in general is that the plasma and its properties are variable not only between tests, but over several pulses as well. With this in mind each voltage level had at least three test fires performed. If the noise levels appeared to change between any runs, an extra test fire was performed.

Figure 4.1 demonstrates how despite the data showing similar behavior, it tended to have large variation in terms of the actual values captured. Using a peak-detection method, it's clear that the peaks occur at slightly different LC times as well as having different peak values. This suggests that the plasma resistance and self-inductance were inconsistent per voltage level test.

A least-squares fit was attempted, but none could suitably capture the decay of the waveform. So a low pass filter was chosen as the best fitting tool for the data. Before doing so however, the test data for multiple runs would be averaged and plotted as $\pm 1$ standard deviations from that mean. This averaged data is then ran through the filter and plotted along side the predicted curves from the RLC model, system (3.6), where the approximate value of $\zeta$ and $L_0$ are extracted from the averaged raw data using a logarithmic decrement approach which is in turn used to calculate $R_c$.

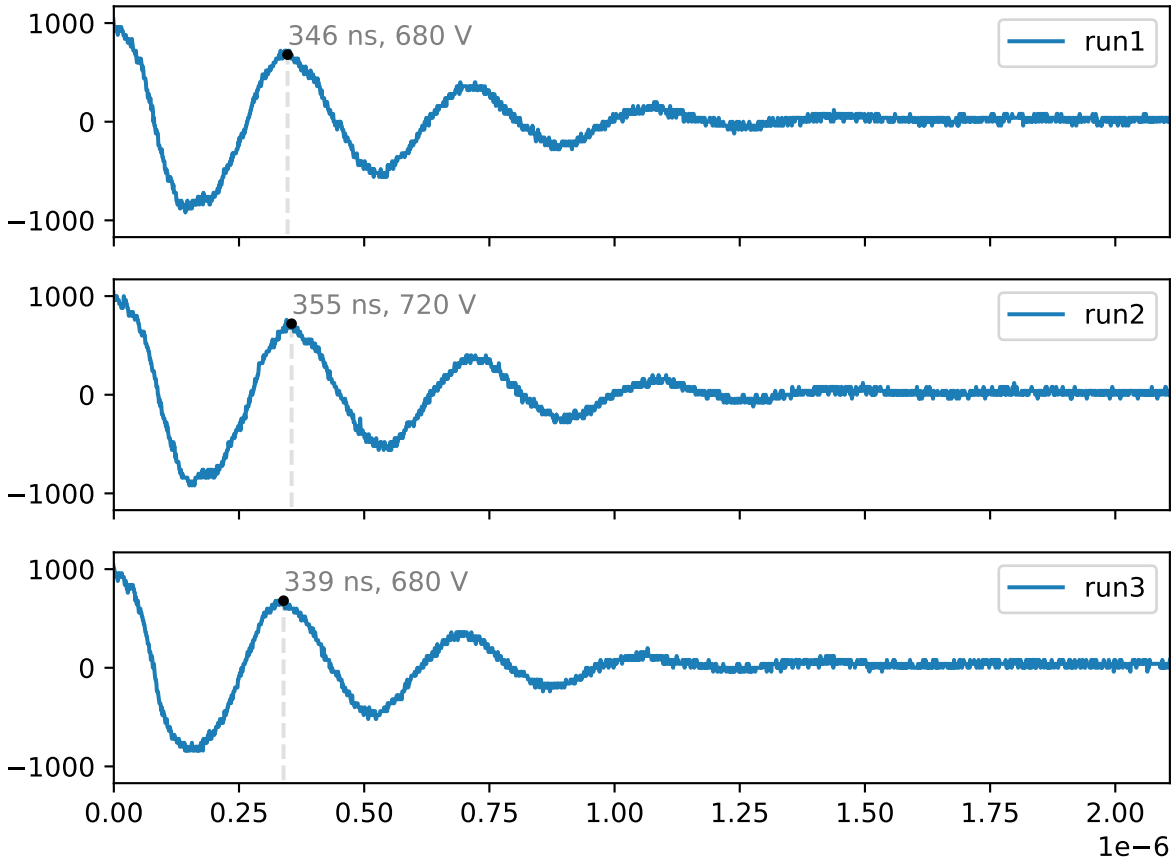


Figure 4.1: A set of raw data from the oscilloscope at $V_0 = 1000$ V.

## *4.2 Oscilloscope Traces*

### *4.2.1 Rogowski Coil*

A rogowski coil was created, tested, and calibrated using a Pearson current monitor but the data produced by it once actually on the PPT was of not much use. The signal was severely attenuated, phase shifted, and only registered positive current implying inductive coupling. It was unknown whether this was due the frequency of the signal being too high for the coil to properly respond or because of the complicated geometry of the thruster.

A sample voltage and current trace which were normalized and plotted for 1000 V is presented in 4.2, where the upper plot shows the two signals shifted over by the same time offset in nanoseconds. Looking at the logarithmic plot, it's clear that even prior to complete discharge there was a tremendous noise signal being generated by something.

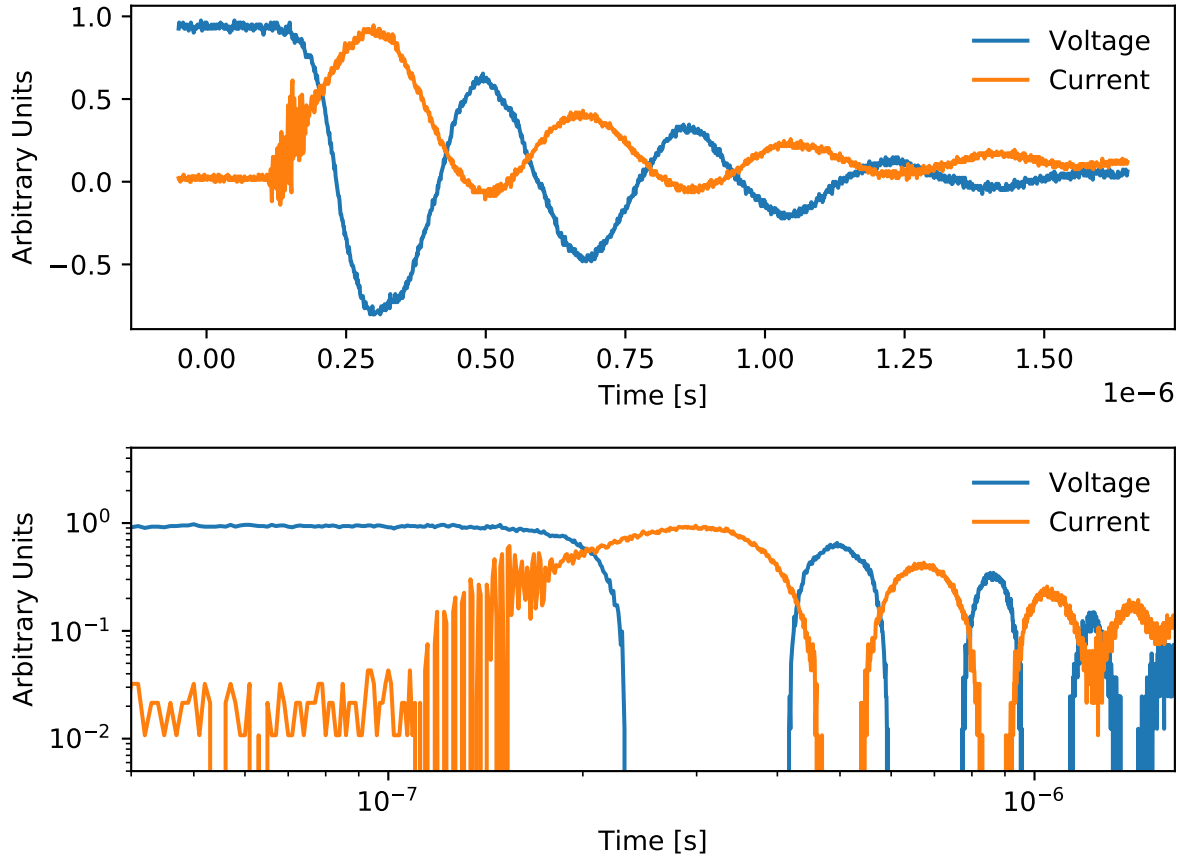


Figure 4.2: Representative plots of the current and voltage traces normalized by max values.

### *4.2.2 1000 V*

The following plots were made for a select set of voltages which showcase the RLC model being compared to the fitted curves and the statistical set of raw data. At this voltage level, one can see that given the information extracted from the averaged data fit, the RLC model captures the behavior of the voltage waveform. The derived current on the other hand seems to be much less damped than that expected from the values returned by the RLC model. If compared to Table 3.4, an expected max current value of 4.85 kA isn't observed from the RLC model which peaks at 4 kA. Likewise, it underestimates the max of the derived current which reaches a peak of 5.7 kA.

Looking at the velocity and position plots, 4.4, it's clear that the model either doesn't fully capture the physics of the plasma or that there are other phenomena at play in the thruster. The expected characteristic velocity at 1 kV should be on the order of 10 km/s but the RLC model and that data estimate are several orders of magnitude off from the estimate. Likewise, the position plots show that the sheet barely moves any distance at all down the channel during the discharge.

### *4.2.3 2000 V*

At this voltage level, the behavior is the same. The information extracted from the averaged data fit, leads the RLC model to capture the discharge waveform very well. Compared to Table 3.4, an expected max current value of 9.70 kA isn't observed from the RLC model which peaks at approximately 7.8 kA. Likewise, it underestimates the max of the derived current which reaches a peak of 10.2 kA. The velocity and position plots still perform poorly in terms of predicting the exhaust velocity and position of the plasma.

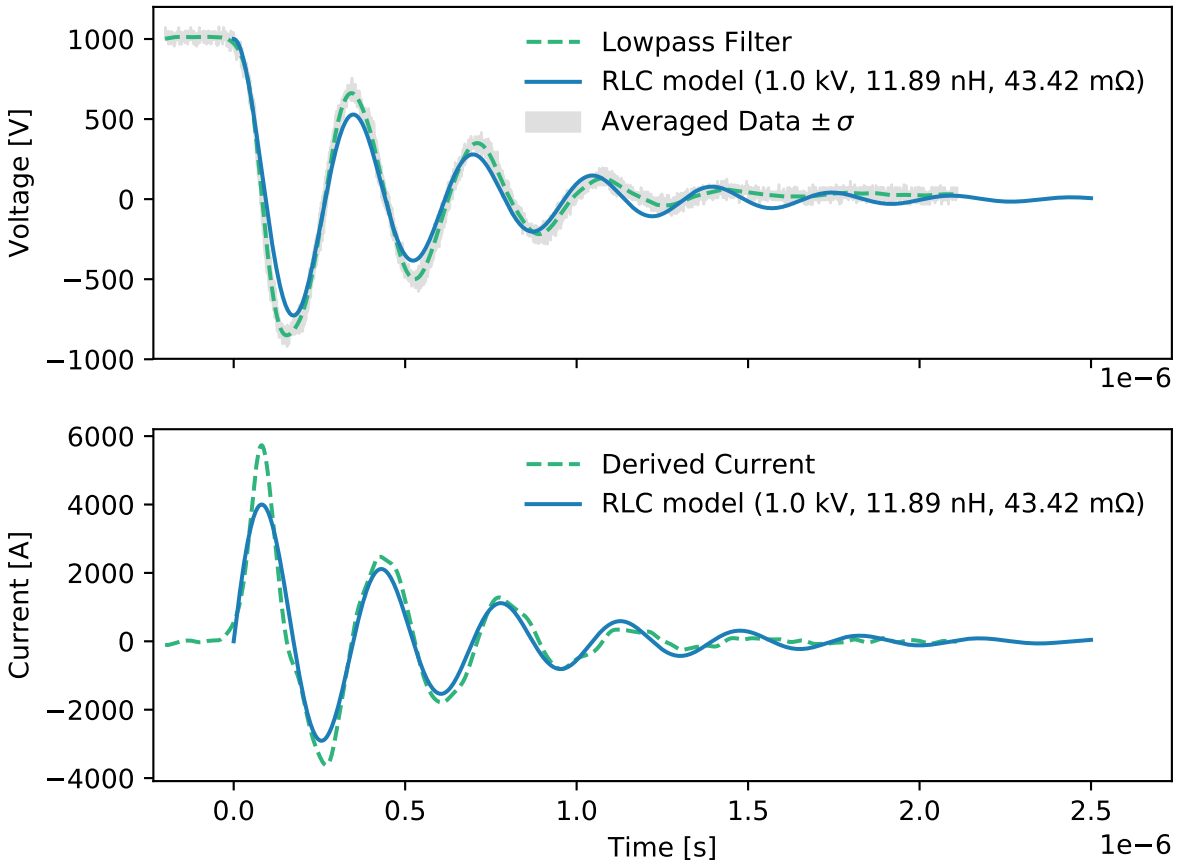


Figure 4.3: Voltage and current plots for a 1000 V test run.

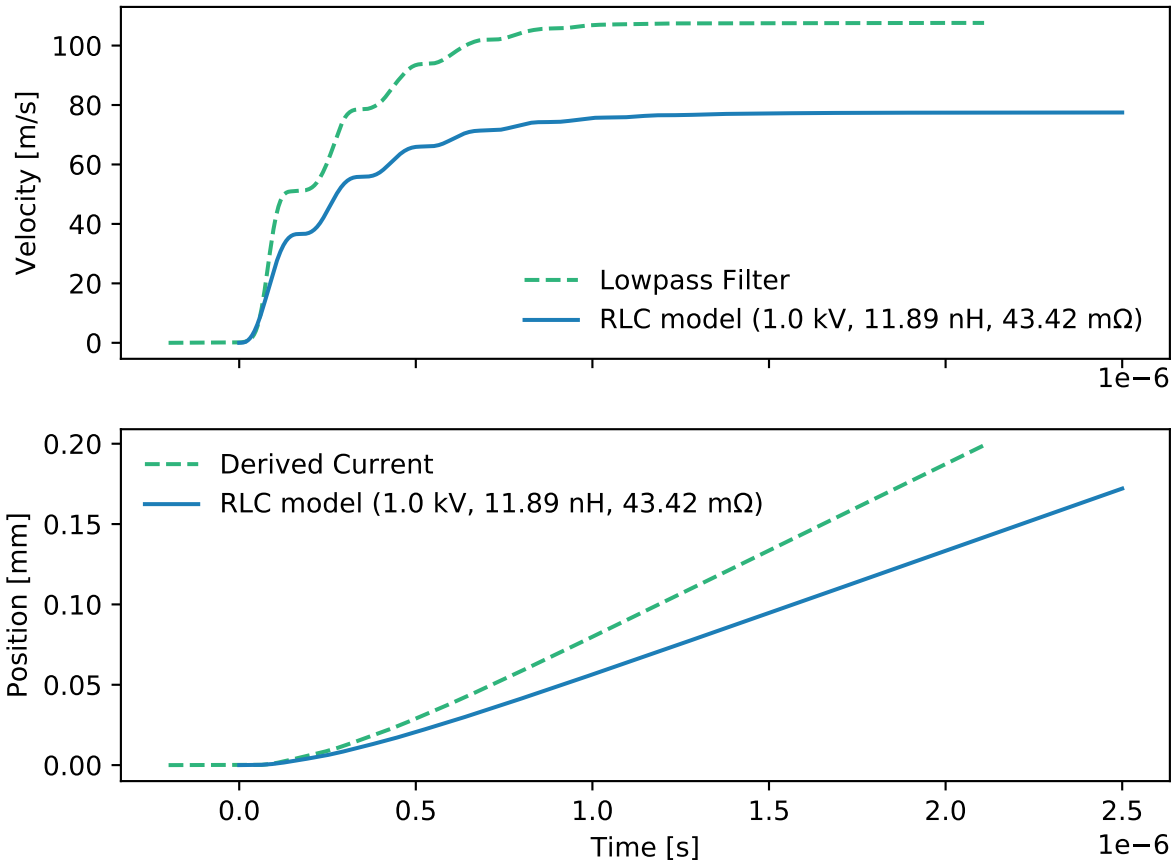


Figure 4.4: Velocity and position plots for a 1000 V test run.

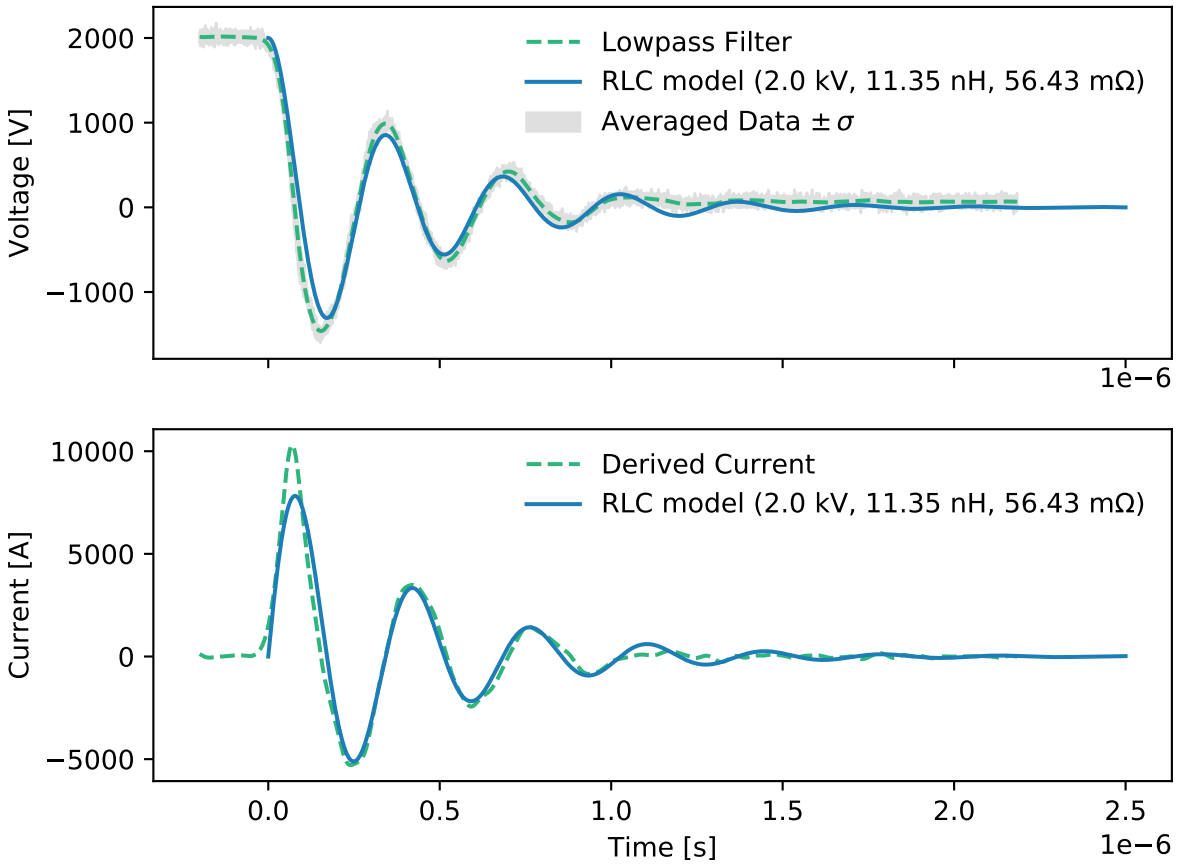


Figure 4.5: Voltage and current plots for a 2000 V test run.

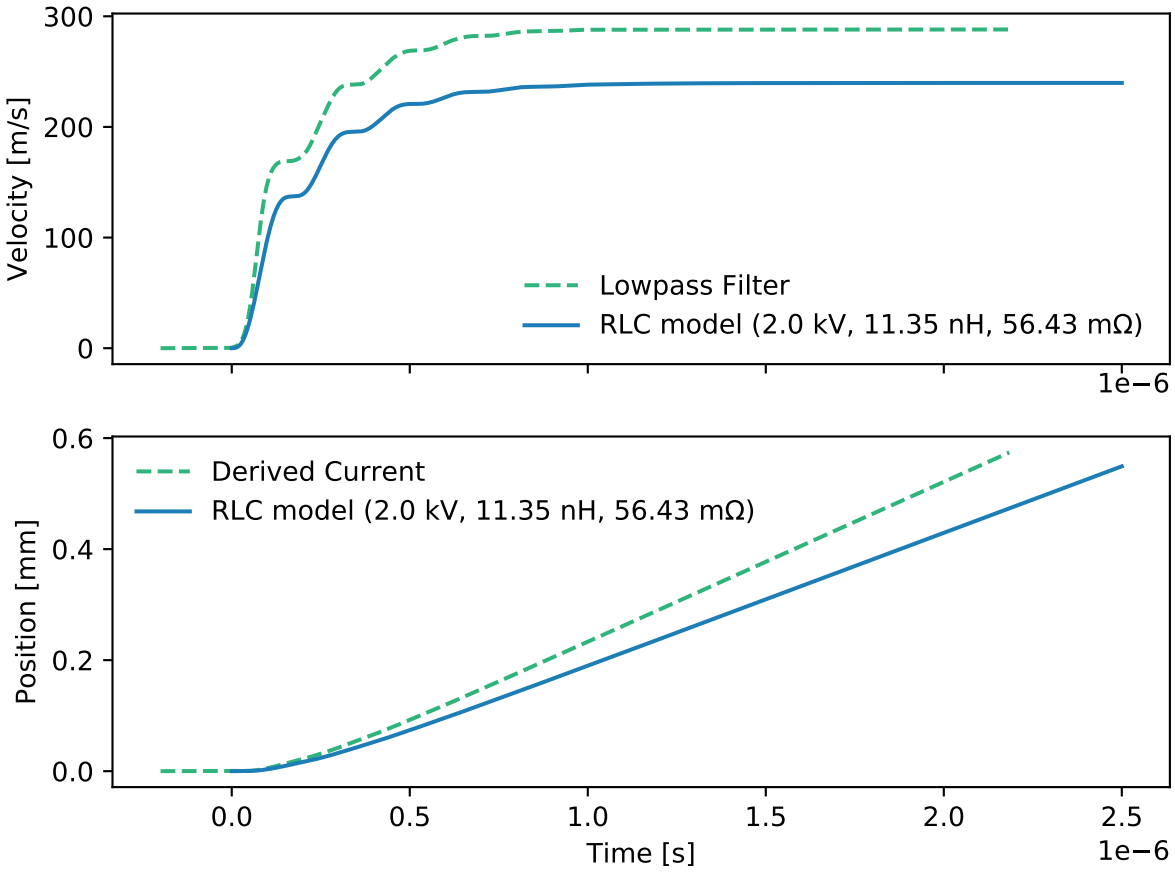


Figure 4.6: Velocity and position plots for a 2000 V test run.

### *4.3 Verifying Wire Breakdown via Experimentation*

The estimated minimum energy required to vaporize the wire was included in the experimental set. This was performed by obtaining the circuit resistance values extracted from the raw data and comparing it to the estimated resistance of the aluminum wire at room temperature. If it was calculated that the resistance of the circuit was greater than that of the wire, no heating considered, then it would be a marker for estimating at what minimum voltage level the wire would vaporize. Using this logic and looking at Figure 4.7, it was found that at approximately 400 V the circuit resistance was about the same resistance of the wire and if the voltage was stepped down to 300 V the equivalent resistance was approximately 110 m$\Omega$.

While this by itself is not strongly indicative of whether the wire vaporized, it should be stated that after every single pulse the thruster channel would be inspected to make sure nothing errant occurred. It was during one of these inspections that for a voltage level of 400 V, that the wire was noticed to have translated down the channel, Figure 4.8. In order to see if this was a fluke, another test pulse at 400 V was repeated and the same event occurred - the wire made it to some downstream distance of the channel. The chamber was also inspected for these tiny wires, but none could be found, suggesting that 400 V was the minimum breakdown voltage.

With this information a rough estimate was carried out using a simple constant parameter heat equation $Q_{heat} = m_{bit}(C_P\Delta T + \Delta H_{fus} + \Delta H_{vap})$ where $\Delta H_{fus}$ and $\Delta H_{vap}$ are the specific heat of fusion and the vaporization enthalpy, respectively, of a substance. Using room temperature values of Aluminum found in [12], [13] , it's estimated that for the volume of wire in the channel an energy amounting to $Q_{heat} \approx 28$ mJ is required. Inspection of Figure 4.7 shows that for a value of 400 V, an initial energy storage of about 10 mJ was the approximate energy range at which the circuit began to exhibit resistance values higher than

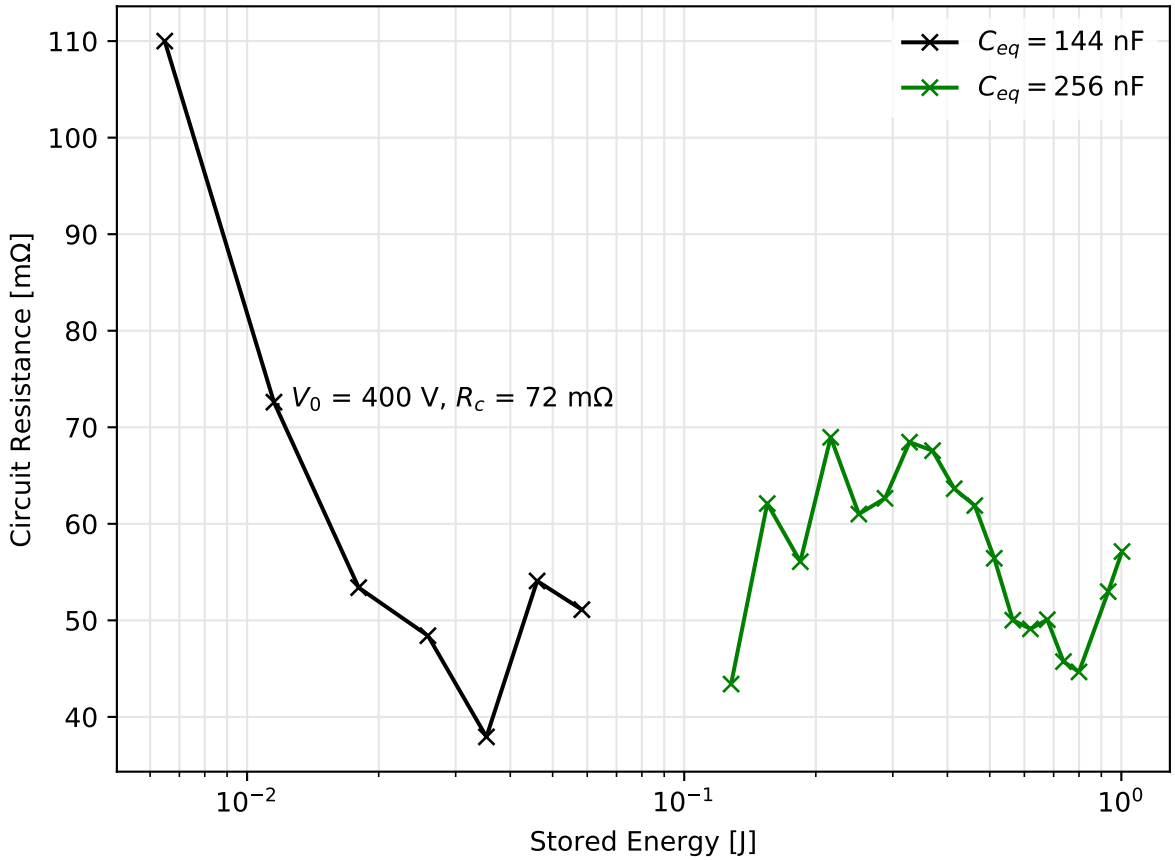


Figure 4.7: Extracted circuit resistance values for varying voltage levels.

the room temperature resistance of the wire.

### *4.4 High Speed Video*

Using a Kirana 5 MFPS high speed camera several shots were recorded to obtain estimates for plasma exhaust velocity, wire ablation time, and general examination of the physics. The main difficulty with using the camera was precisely capturing the full pulse process and ensuring the right exposure settings were used. This proved difficult as the camera seemed to have a cutoff signal strength on the sensor and closing the aperture past a certain point would

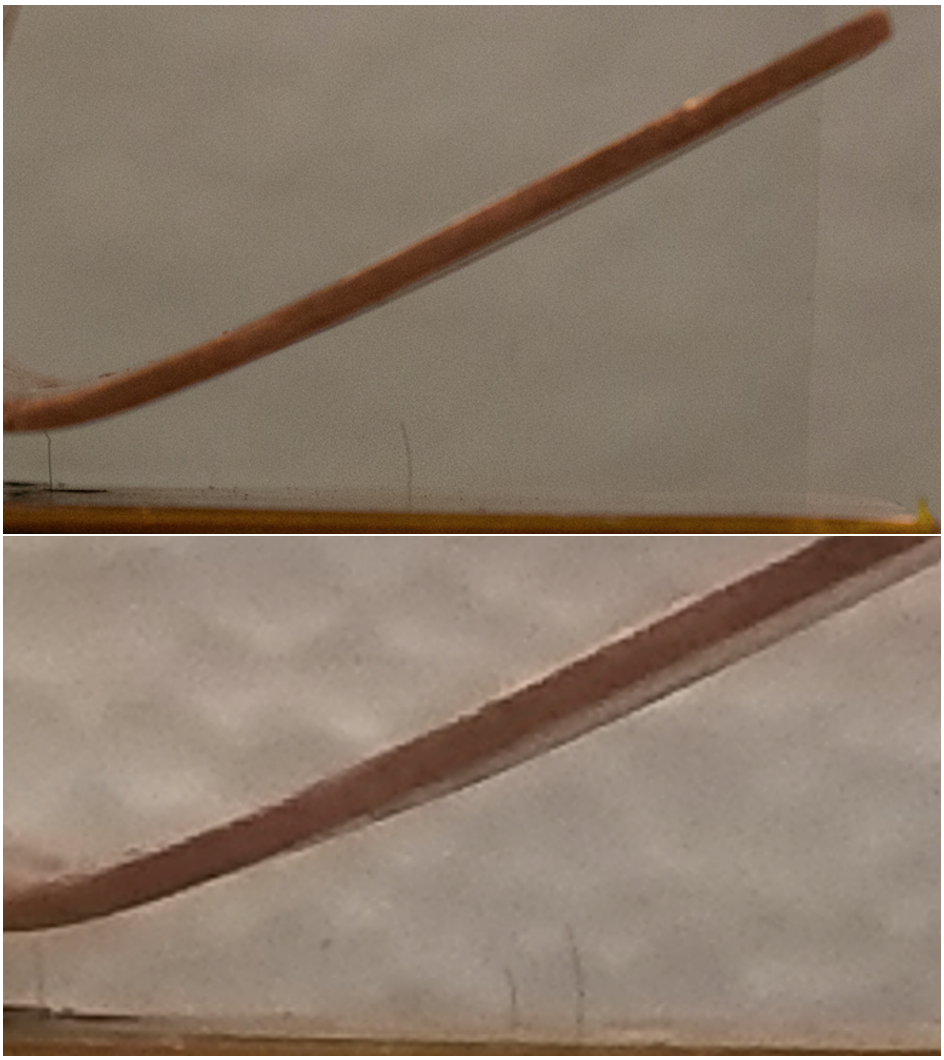

Figure 4.8: Captured image of wire bit not ablated and pushed downstream of the throat by approximately 10 mm. Wire bridging both electrodes shown for scale.

produce no images. Even just at the cutoff point, the sensor was still being oversaturated with light. This created ghosting artefacts which appear on screen as "ghostly" pulses of the event captured, but in decaying light intensity until it disappeared. In other words, bright flashes would remain on the sensor and continue to exist well after their occurrence, but at a much less luminous level before fading away. So in order to quantify anything using the camera, relative changes between each frame were used and only bright events were considered in interpreting the results.

Examining the series of images in Figure 4.9 one can see that the lack of any new, bright defining features and the relative shrink in volume of the plasma between frame five and six indicates that no new phenomena was being captured and only the artefacting of the sensor was occurring. Using this, then somewhere between frame five and six is anything new being captured. It's estimated that the total pulse duration was $0.8\,\mu\text{s} \leq t_{pulse} \leq 1.0\,\mu\text{s}$ which matches the oscilloscope data. Now, looking at the first two frames, one can see in the first frame that either surface imperfections, or leftover aluminum particles, were being illuminated via dielectrical breakdown well before the wire shorted the circuit, indicative of energy losses. By the next frame, 200 ns had ellapsed and the wire had already been destroyed. This is a good indication that the first order and numerical estimate wire vaporization times are at least true in that they happen in the low end nanosecond time scale. This information could not have been gleaned from the oscilloscope data.

Looking at Figure 4.10, the next two frames in the sequence catch the initial act of the current running through the wire. It is interesting to see this captured because it essentially shows the wire very rapidly heating and emitting visible light. Likewise, the same frame appears to show the first evidence of super heated matter. It is either heated aluminum nanoparticles being ejected outwards due to evaporation, because of the low boiling pressure, or the explosive expansion of the wire in the process of its vaporization.

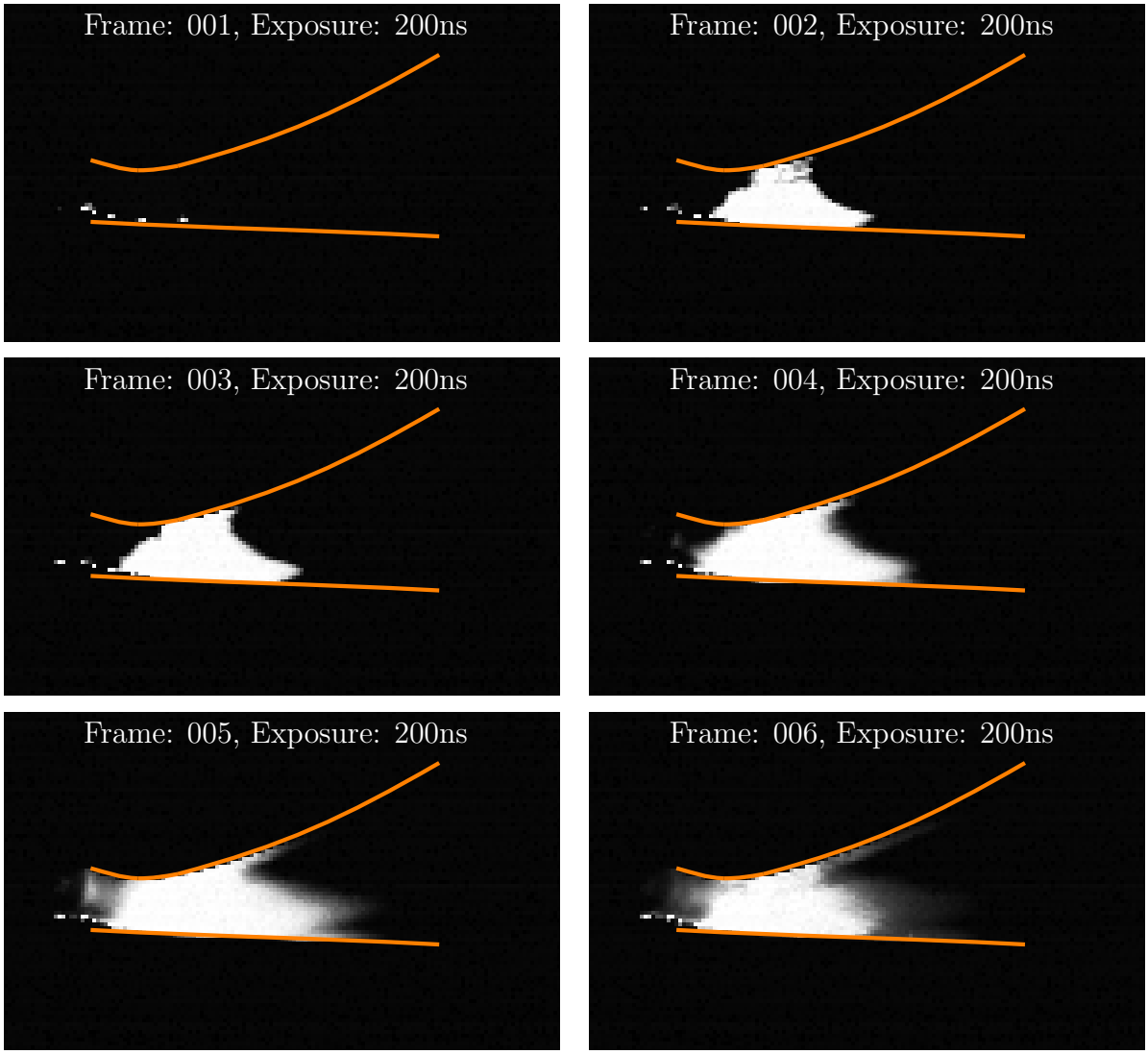


Figure 4.9: Wire breakdown process, 2000 V, captured by high speed video.

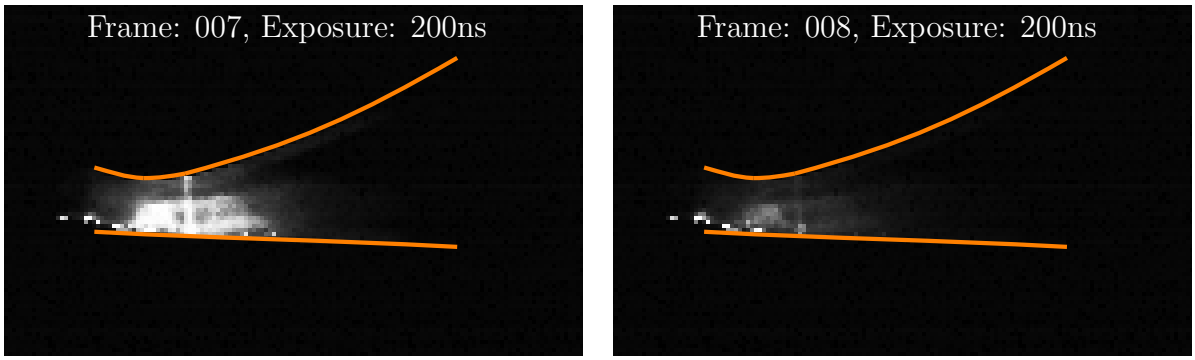


Figure 4.10: Wire breakdown process, 2000 V, captured by high speed video.

The next sequence of images are captured at the same frame rate, but with more light permitted through the aperture. Examining Figure 4.11 one can see that by the second frame the plasma is already traversing down the channel. It continues accelerating and come frame seven it reaches the end of the capture process because on frame eight the plasma has accelerated out of the thruster and no new discernable boundaries are visible. Between frames six and seven, rough approximations of the thruster channel length, and the location of the plasma leading edges are included in the figures. Since the plasma is almost out of the channel at this point in time, it could serve as a good estimate on exhaust velocity. Having translated approximately 2 mm in the span of approximately 400 ns, it provides a lower bound on the velocity using the frame-by-frame analysis. This estimates the plasma leading edge as traveling at least 5 km $s^{-1}$ near the end of the thruster.

## *4.5 Comparing Raw Data to Scaling Laws*

Having performed the analysis described in the previous sections, both sets of data are plotted in Figure 4.12. The current scaling estimates are well-bounded by the data obtained by both the RLC model and the data-derived current.

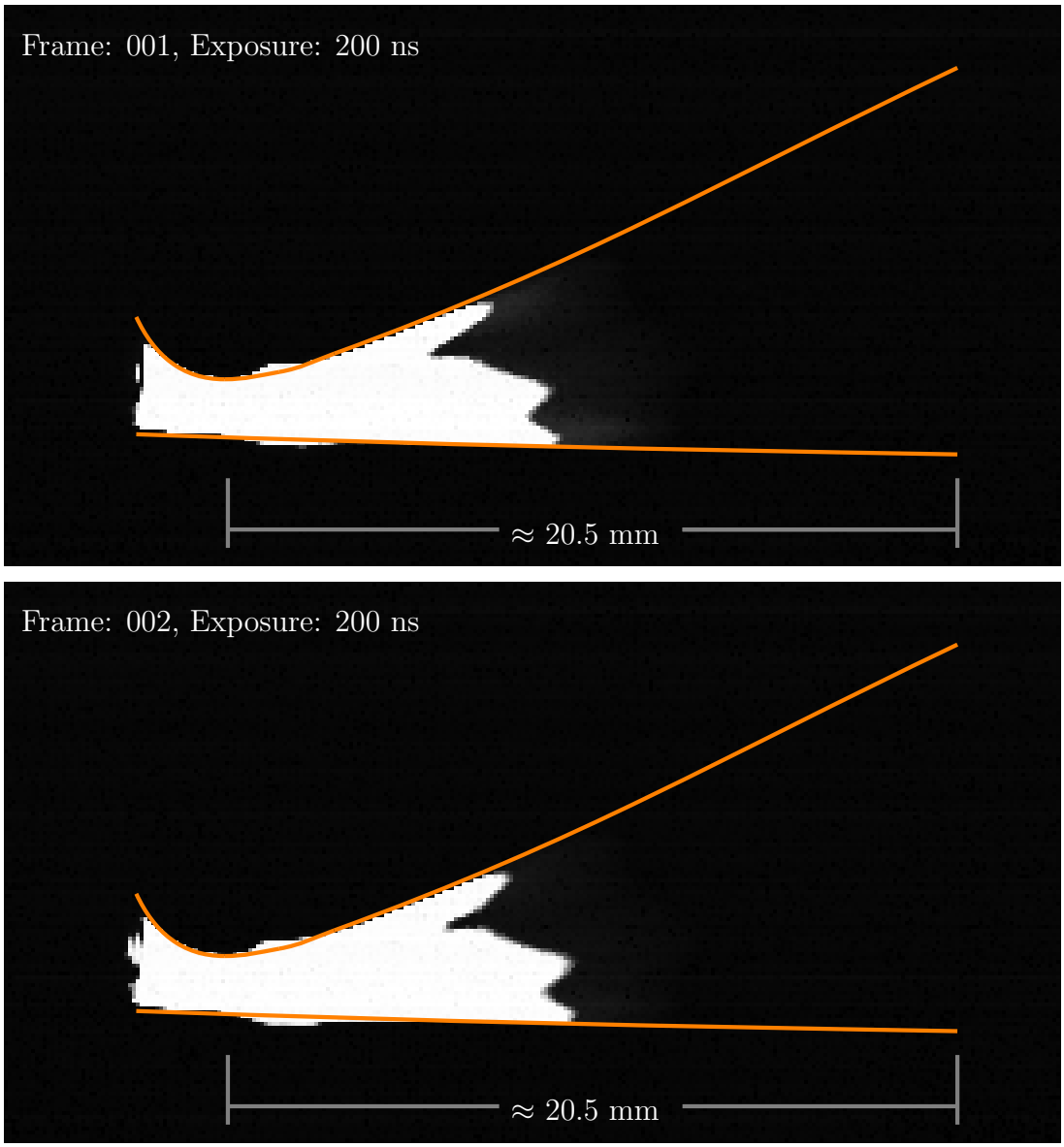
Frame: 001, Exposure: 200 ns
≈ 20.5 mm
Frame: 002, Exposure: 200 ns
≈ 20.5 mm

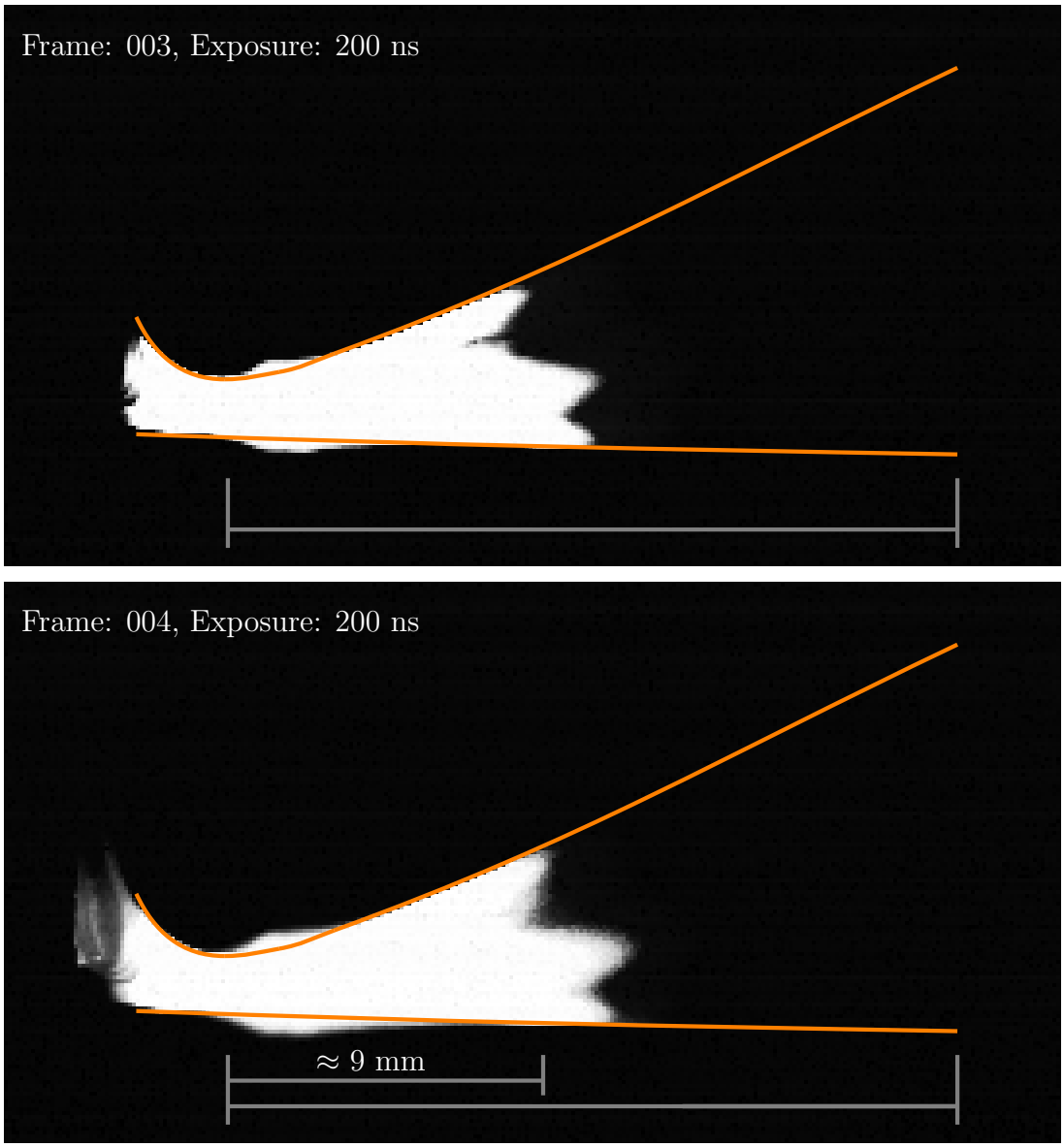
Frame: 003, Exposure: 200 ns
Frame: 004, Exposure: 200 ns
≈ 9 mm

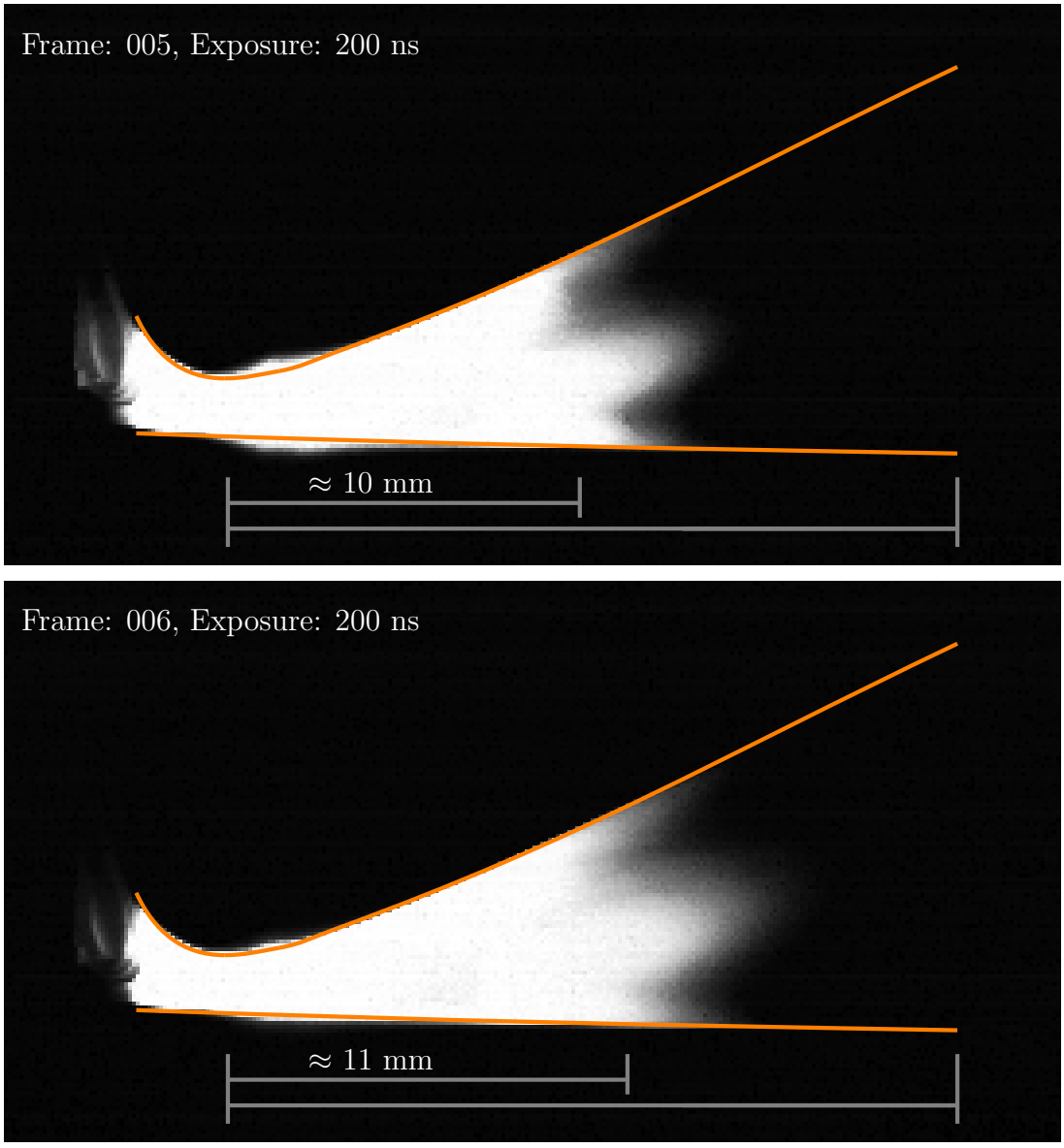


Figure 4.11: Still images of the plasma accelerating down the channel using the Kirana at 5MFPS with a voltage of 2500 V.

What is unfortunate is the very low resulting velocity estimates obtained from the frame-by-frame footage analysis. This is likely due to a culmination of a mass-utilization issue with the thruster, a higher ratio of electrothermal to electromagnetic processes, and a failure of the camera to provide good visual reference because of poor sensor detection capability of self-illuminating processes. Inspecting the data in Figure 4.12, it's apparent that between theory, scaling, and modeling there is a significant gap between each of the data sets – each an order of magnitude apart. In the proceeding section this difference is explored by considering alternate physics.

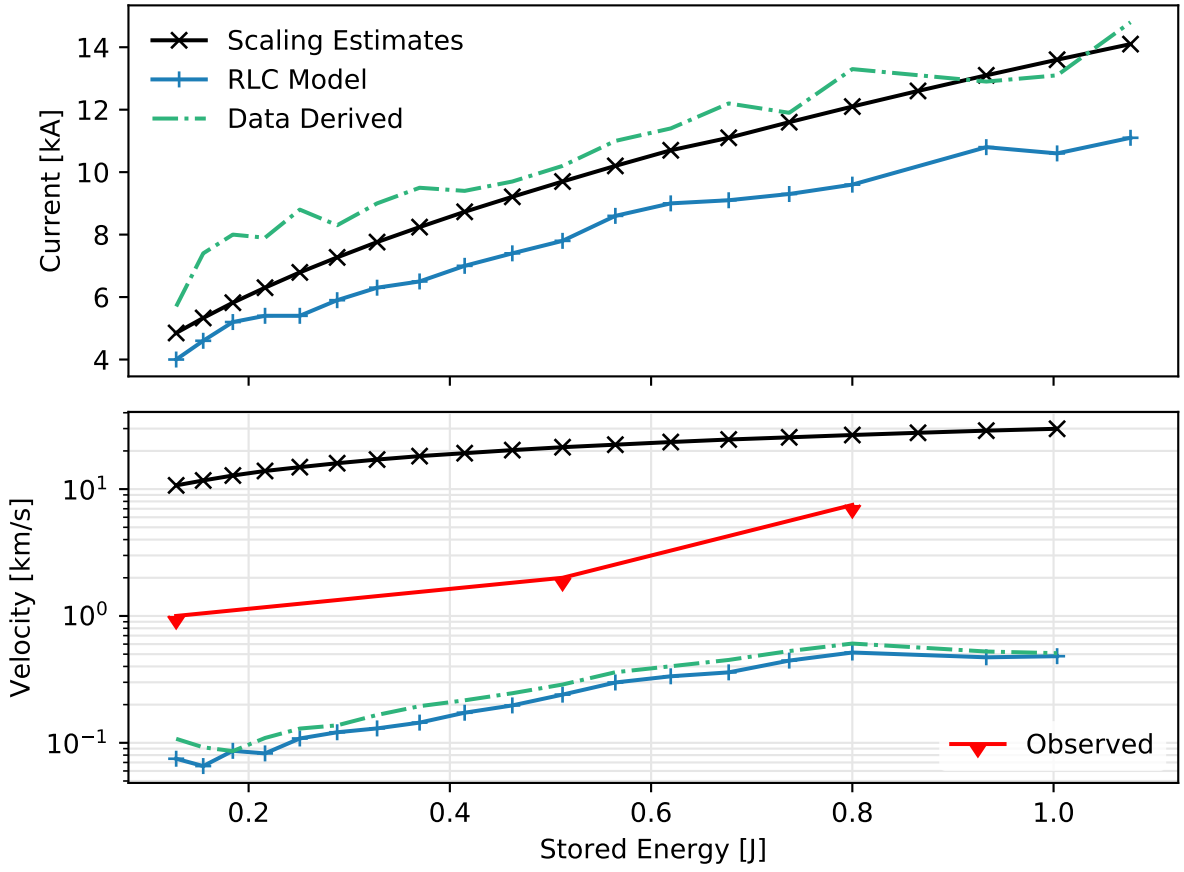


Figure 4.12: Visual comparison of performance differences between theory, modeling, and experimentation for expected currents and velocities.

## *4.6 Critical Analysis*

The main crux of this experiment was to set out to prove the exploding wire method could be approximated with a traditional PPT RLC circuit model, that vaporization could occur on a timescale significantly less than the characterizing circuit periods, and prove that this new propellant type could be usable in future missions. The next step is to now analyze the results obtained and see what parameters could be modified in the model to produce the results seen in the experimental outcomes.

### *4.6.1 Mass Utilization*

During the testing of the thruster it was noticed that a silvery, metallic deposition was building up on the glass slides. It started accumulating after a handful of test runs, leaving a side-view impression of the exhaust channel as seen in Figure 4.13. While a complete mass utilization ratio wasn't expected, the resulting velocity estimates from the integrated data and the RLC model strongly hinted that since only equation 3.6's velocity component depended on the expended mass $m_{bit}$, then much less mass than was entered into the throat of the thruster was being utilized.

With this in mind, the variable $m_{bit}$ was manipulated in the raw data integration such that it produced a resultant velocity in the same range as that found via camera analysis for the 1000 V, 2000 V, and 2500 V test runs. By performing this, it was found that for the 2500 V test a mass utilization of approximately 14% would produce results to match the data. In other words, of the total mass entering the channel to be ionized, only a seventh of it was estimated to be utilized. This helped to produce a similar exhaust velocity, see Figure 4.14. This was also performed for the other two voltages and as seen in Figure 4.15, it's noticed that the mass utilization fraction hovers at the 10% range, but much more data would be required to establish a more concrete relationship with increases in voltage. Also in this plot are the recorded velocities to show how the mass utilization growth rate compares

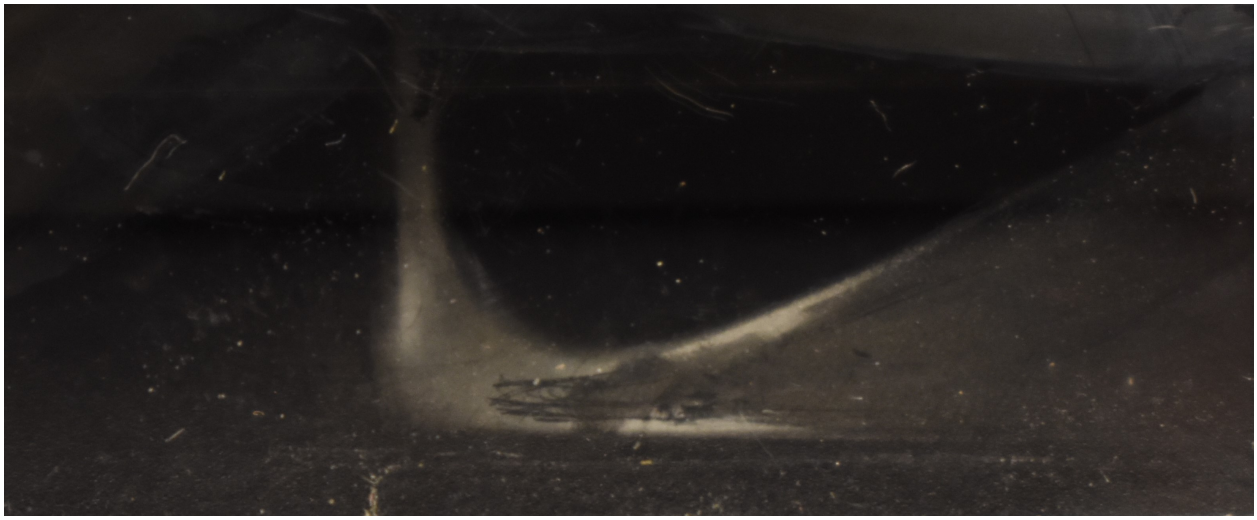

Figure 4.13: Metallic aluminum powder built up on the slides after several test pulses.

to them. Looking back at Figure 4.12, if the mass utilization assumption is correct, then both the RLC model and derived velocity data would shift upwards towards the observed velocities and further reduce the disparity between that estimated by scaling laws and what was observed. It would be beneficial to explore this relationship further to see if hitting a certain utilization rate would limit the maximum exhaust velocities a micro-wire PPT could obtain. Likewise, perhaps past a certain point of energy input to the thruster would one start seeing net increases in efficiencies.

### *4.6.2 Electrothermal Dominance*

Another consideration that was taken into account was that perhaps the low velocities seen from the model were due to the wrong acceleration force being taken into account. If instead the dominant force seen by the plasma was that experienced by an electrothermal thruster, then another equation needs to be taken into account. Assuming a predominantly electrothermal process and that the plasma can be modeled as a simple one-dimensional, isentropic, adiabatic flow, then the energy balance can be written as

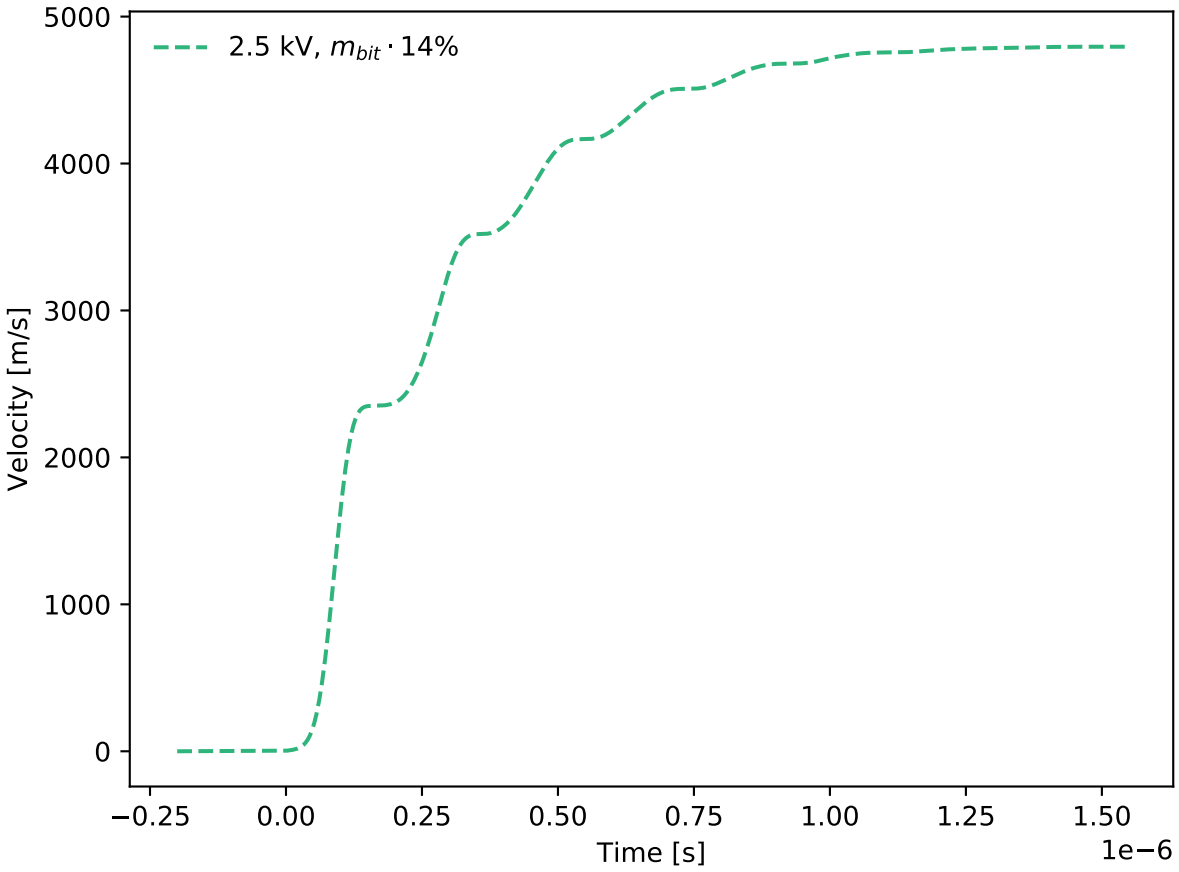


Figure 4.14: Manually taking into account an estimated mass bit utilization factor, the estimated velocities could be reproduced.

$$h_0 + \frac{1}{2}v_0^2 = h_e + \frac{1}{2}v_{ex}^2$$
$$v_{ex} \approx \sqrt{2C_pT_0}$$

Where $T_0$ is the initial temperature of the gas prior to acceleration. Continuing from the initial assumption of a $T = \mathcal{O}(1)$ eV plasma, and assuming that the maximum value of

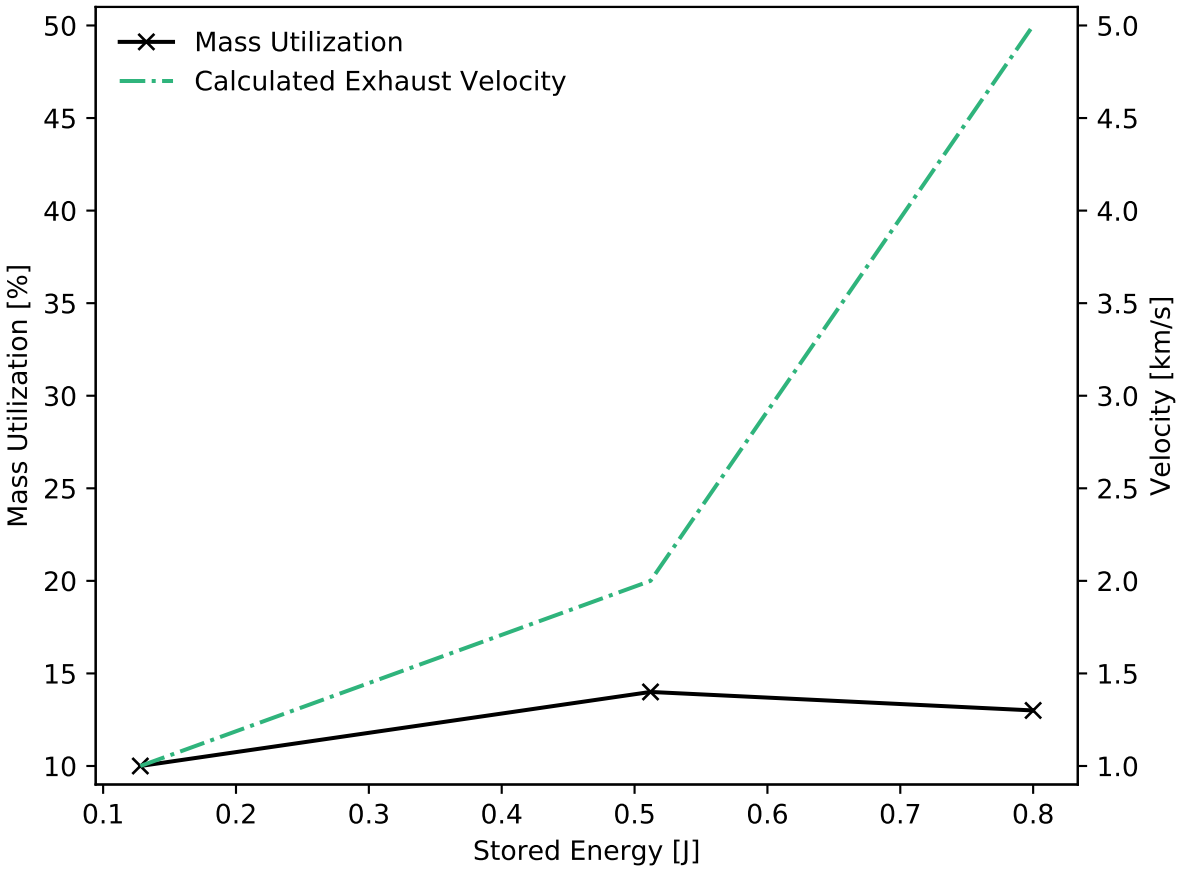


Figure 4.15: Raw data points showing mass utilization percentages that can reproduce the velocities calculated from camera footage analysis.

specific heat is $C_P = 1200$ J kg$^{-1}$ K$^{-1}$, then a velocity estimate of $v_{ex} \approx 5.3$ km s$^{-1}$ is calculated. This velocity estimate also appears to account for the disparity seen between the recorded data and the footage analysis. However, this fails to be accurate for the lower voltages because in order to reproduce the 1 kV and 2 kV velocities, temperatures less than the boiling point of Aluminum would be necessary which falls out of the realm of possibilities.

### *4.6.3 Efficiencies*

One of the first measures considered was how efficient the thruster was at converting the given initial electrical energy for a given voltage, and how well it did at transforming that into useful acceleration. This is expressed as

$$\begin{aligned}\eta_W &= \frac{K.E.}{W_0} \\ &= \frac{m_{bit}\, v_{ex}^2}{C\, V_0^2}\end{aligned}$$

Where the numerator is the final kinetic energy of the exhaust plasma and the denominator is the initial electrical energy stored in the capacitor bank. Another efficiency proposed is found in [7] where it posits that another measure of defining one is

$$\eta_E = \frac{\Delta L}{L_0}$$

Where the total change in inductance over the pulse, $\Delta L$, should be comparable to that of the initial inductance of the circuit, i.e., $\Delta L/L_0 \approx 1$. This implies that a violation of this is indicative of high losses due to resistances or an uncoupling of the plasma from the exhaust channel prior to complete capacitor drain. The former implying that the residual energy is either left in the capacitors or lost in the stored electromagnetic field energy carried away by the plasma. This is both tabulated for sample voltages in Table 4.1 and for the full voltage range in Figure 4.16. The electrical efficiency plot has a lot of jumps and doesn't appear to show a specific trend other than appearing to increase as the voltage increases, so more data would need to be collected a higher range of voltages. As expected, the poor performance of the thruster in converting stored energy into useful, directed momentum change of the plasma led to hindrances in the efficiency of the thruster.

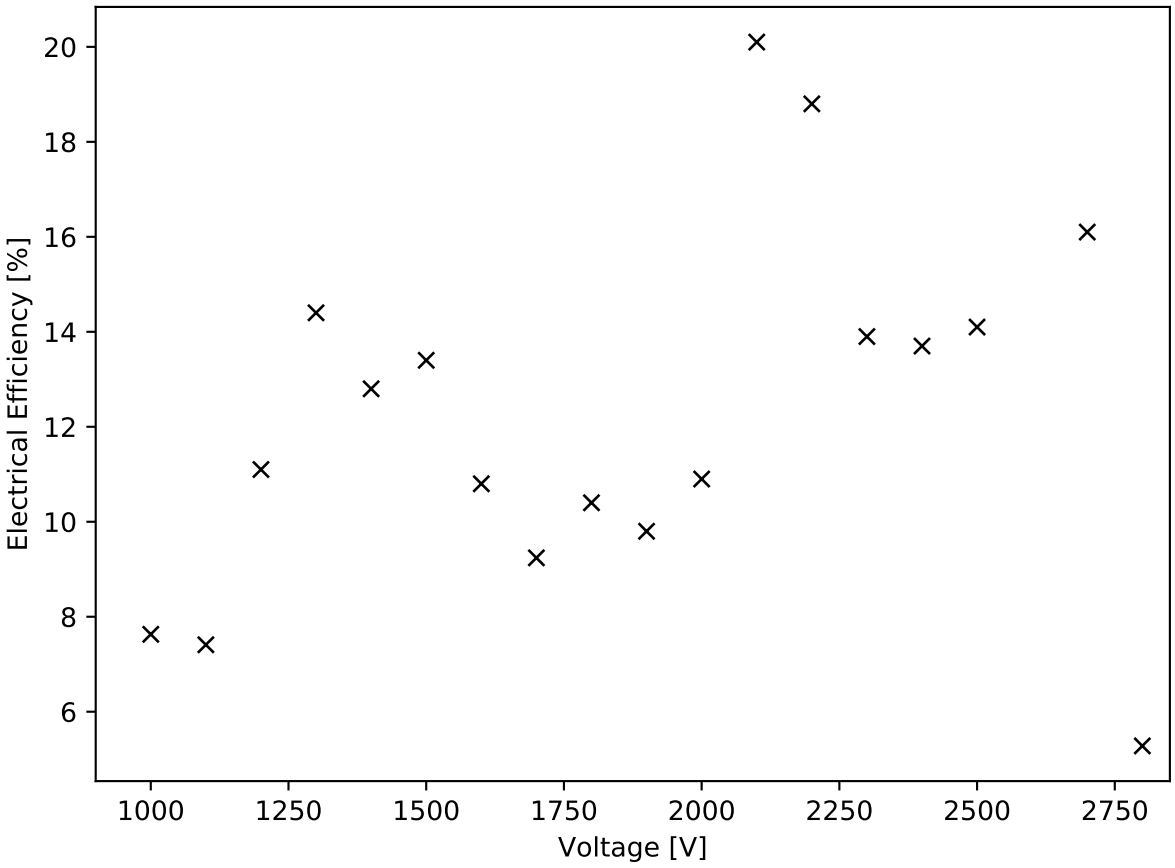


Figure 4.16: Data points for electrical efficiency as a function of voltage.

Table 4.1: Comparison of the different efficiencies of the thruster.

| $V_0$ | $\eta_W$ | $\eta_E$ |
|---|---|---|
| 1000 | 0.8% | 12.7% |
| 1500 | - | 13.4% |
| 2000 | 0.8% | 10.9% |
| 2500 | 1.2 % | 5.21% |

### *4.6.4 Impulse Bit*

The impulse bit for the thruster was calculated using the final velocity of the thruster and the mass of the wire expended in a single pulse. Figure 4.17, shows what the expected scaling estimates would yield as well the estimates obtained from the RLC model and the raw data. Now, using those velocities observed from the high speed camera, it's clear that once again there seems to an order of magnitude difference between each of the curves. However, if the mass utilization factors from Figure 4.14 are considered, then a corrected impulse bit curve is generated which falls directly in line with that observed in the models – mass correction also included.

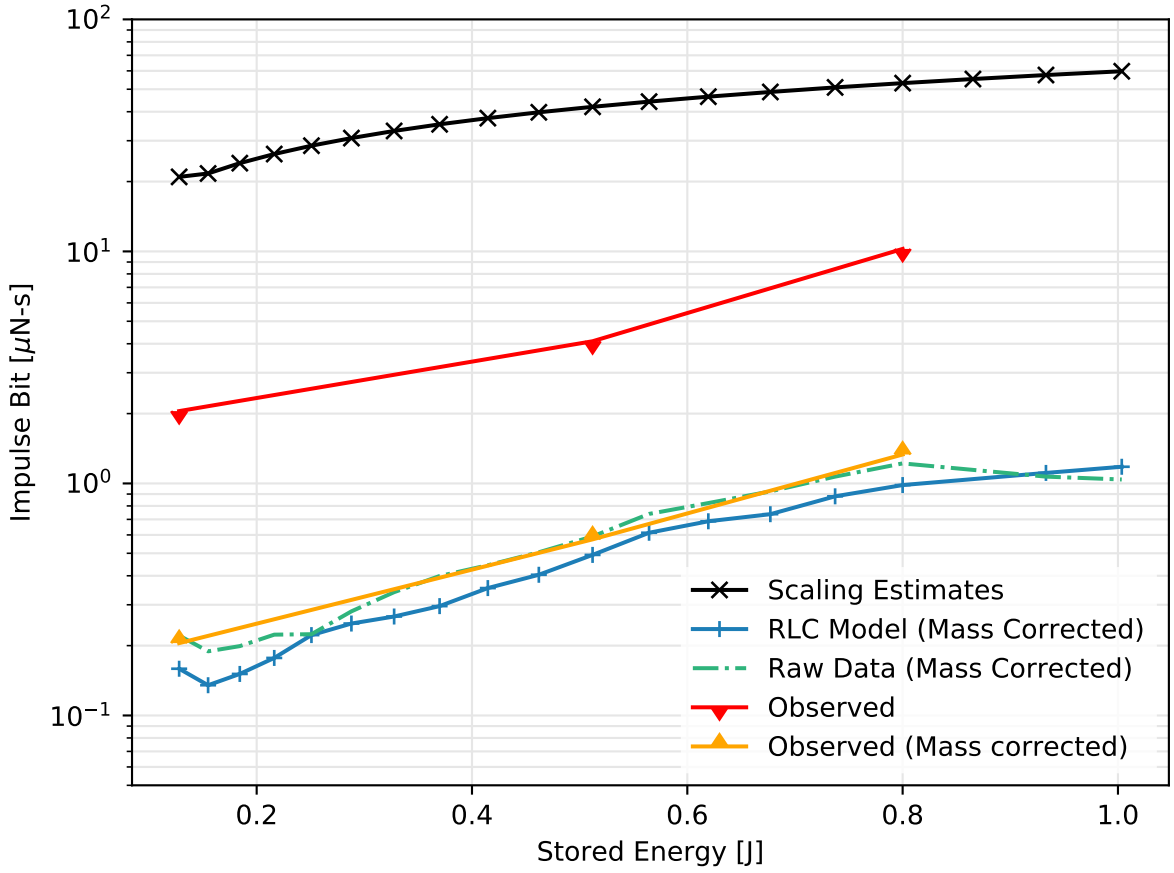


Figure 4.17: Impulse bit calculations from scaling table, raw data, RLC model, and observed velocities.

# Chapter 5

# CONCLUSION

In the end, the thruster did succeed in helping establish that to first order, a wire's ablation time could be estimated using both analytical and numerical techniques. In terms of performance, its current and exhaust velocities could be predicted from both probe measurements and high speed video analysis. Using both predicted and calculated values, thruster efficiencies were calculated and shown that for the configuration setup and geometry of the experiment, that very low yields of energy conversions were occurring. Likewise, by thinking of other possible physics processes that may have occurred it was found that experimenting with values of consumed mass could be a possible explanation for the low yields in velocities. Electrothermal effects could also help account for the performance issues of the thruster.

In future work, it would be suitable to explore solutions to the three major hindrances that contributed to the inconclusiveness of the data presented herein. The first being that the rogowski coil was not useful in providing any meaningful data. As mentioned briefly, it was suspected that the self-inductance and self-capacitance of the coil, alongside its location on the thruster, helped to produce an indiscernible signal from which no meaningful information could be extracted. There could be future time invested into determining whether it was also the frequency of the signal that lended to the ill-defined curve produced as even rogowski coils have cut-off frequencies at which they can effectively respond to. Simply put, complex geometry, nanosecond response time, and proper calibration and integration of the coil signal all have to be considered for a wire-fed pulsed plasma thruster.

The second contributor to difficulties in this experiment lied with the high speed footage.

Rather than relying on data, models, and theory to produce a velocity estimate, the camera could have provided a very direct measure of plasma exhaust velocity. The downside is that the sensor itself has sensitivity issues if no external light sources are illuminating the process being captured. Since the plasma generates its own light, the sensor would only be able to respond to the brightest portions of the plasma that were most prominent in a single frame exposure. To go along with this, the camera itself also had a troublesome issue with not properly shutting off the sensor's pick-up signal if overexposed, i.e., the artefacting problem encountered. A lot of the analysis relied on ensuring that no two frames were alike, that no event was being erroneously displayed by the sensor moments after it already happened, and that boundaries used in the calculation were truly representative of the plasma edges at that given instance in time rather than being the brightest remnants caught in a single frame.

Lastly, the feeding mechanism and the wire thinness combined presented great difficulty in terms of being able to pulse the thruster consistently and without pause. The wire would continuously get stuck inside the guide tube after a handful of test fires and fail to enter the channel and start bending. This in turn led to several deconstructions of the test chamber and the experiment setup, and introducing contaminant exposure to the system as the wire then had to be reintroduced manually into the guide tube and gently prodded so that it could feed through once more.

Now considering future work in the context of how the experiment itself could be improved would be to start off with a more compact design where the feed mechanism is smaller and less prone to stopping the wire midway through the guide tube. Likewise, the motor used was the heaviest component of the whole experiment and could be downsized significantly. How the capacitors were soldered could also be improved. Making a clean solder connection between the copper plate and the capacitor leads proved difficult and voids were left in some sections. This wasn't apparent until watching high speed footage or looking at long-exposure photographs where arcing occurred between tiny gaps. These represented losses since energy

had to be expended in order for the electrons to complete the jump through vacuum.

Another improvement would be to better contain the plasma to the channel and prevent leaks. The glass slides were non-permanently attached to the thruster so they could be changed out if needed, but this also let some plasma slip through the small crevices which is apparent from the movie frames. As mentioned before in the discussion of the electrical efficiency, plasma decoupling signifies a loss as the plasma volume prematurely leaving the channel meant that electromagnetic energy in its field was being carried away with the mass bit. Another source of premature plasma escape was through the wire guiding tube. Since the wire was the short of the whole circuit, then from the instance the plasma is created, some of it had means to escape before even accelerating through the channel. This is also apparent from the high speed stills obtained from the video footage.

Finally, in consideration of further diagnostics to help more concretely characterize the thruster would be the use of a thrust stand. One was calibrated and available, but by that point two of the capacitors had failed and further testing would've likely damaged the other two as well. Another useful measurement would be to use spectroscopy analysis to determine the energy levels of the plasma. This could thereby help in deducing what ionization states were present in the cloud. This could then indirectly give insight into how much useful energy was being used to accelerate the plasma rather than wasting energy in creating higher ionization states of Aluminum. This was attempted, but given the discharge window of 1 $\mu$s it was a difficult process to capture. Especially so since a typical exposure window on the order of hundreds of milliseconds also had to contain the plasma discharge window. To go along with this, even if the event was captured there was too much noise for any discernible signal to be made out among the noise.

# BIBLIOGRAPHY

[1] NASA Pulsed Plasma Thrusters. https://www.nasa.gov/centers/glenn/about/fs23grc.html. Accessed: 2019-04-10.

[2] Rodney L. Burton. *Pulsed Plasma Thrusters.* Encyclopedia of Aerospace Engineering, AIAA, 2010.

[3] W. J. GUMAN and P. E. PEKO. Solid-propellant pulsed plasma microthruster studies. *Journal of Spacecraft and Rockets*, 5(6):732–733, 1968.

[4] Hiroyuki Koizumi, Yohei Furuta, Keiko Watanabe, Kimiya Komurasaki, Akihiro Sasoh, and Yoshihiro Arakawa. A pulsed plasma thruster using water as the propellant. 07 2004.

[5] Zhe Zhang, William Yeong Liang Ling, Junxue Ren, Haibin Tang, Jinbin Cao, Xin Lin, and Thomas M York. The plasma morphology of an asymmetric electrode ablative pulsed plasma thruster. *Plasma Sources Science and Technology*, 28(2):025008, feb 2019.

[6] D. J. Palumbo and W. J. Guman. Effects of propellant and electrode geometry on pulsed ablative plasma thruster performance. *Journal of Spacecraft and Rockets*, 13(3):163–167, 1976.

[7] Robert G. Jahn. *Physics of Electric Propulsion.* Dover Publications, 1968.

[8] D.A. Kaminski and M.K. Jensen. *Introduction to Thermal and Fluids Engineering.* Wiley, 2005.

[9] W. J. Parker, R. J. Jenkins, C. P. Butler, and G. L. Abbott. Flash method of determining thermal diffusivity, heat capacity, and thermal conductivity. *Journal of Applied Physics*, 32(9):1679–1684, 1961.

[10] Matthias Leitner, Thomas Leitner, Alexander Schmon, Kirmanj Aziz, and Gernot Pottlacher. Thermophysical properties of liquid aluminum. *Metallurgical and Materials Transactions A*, 48(6):3036–3045, Jun 2017.

[11] P. D. Desai, H. M. James, and C. Y. Ho. Electrical resistivity of aluminum and manganese. *Journal of Physical and Chemical Reference Data*, 13(4):1131–1172, 1984.

[12] G. R. Gathers. Thermophysical properties of liquid copper and aluminum. *International Journal of Thermophysics*, 4(3):209–226, Sep 1983.

[13] Edgar H. Buyco and Fred E. Davis. Specific heat of aluminum from zero to its melting temperature and beyond. equation for representation of the specific heat of solids. *Journal of Chemical & Engineering Data*, 15(4):518–523, 1970.

[14] R.J Goldston and P.H Rutherford. *Introduction to Plasma Physics*. CRC Press, 1995.